

Ward, Lyndee Higgs, Assessing Ecogeographical Variation in the Nasal Passages Utilizing 3D Semilandmarks. Master of Science in Medical Sciences – Anatomy, May 2021. 57 pp., [15] tables, [26] illustrations, bibliography [48] titles.

Prior research has shown strong statistical relationships between geographically-patterned variation in nasal skeletal morphology and global climatic conditions. Specifically, the nasal skeletons of individuals indigenous to cold-dry environments tend to be longer, taller, and especially narrower, than those from hot-humid environments. As the nasal passages heat and humidify inspired air for entry into the lungs, this morphological patterning is believed to reflect the specific air-conditioning demands of different climates. However, while it is widely assumed the morphology of the nasal skeleton accurately reflects that of the functional (soft-tissue) nasal passages, the existence of ecogeographic variation in the three-dimensional (3D) nasal soft tissues has yet to be empirically demonstrated. This study investigates 3D shape variation in decongested soft-tissue nasal passages of individuals ancestrally derived from cold-dry (CD) and hot-humid (HH) environments ($n=20$). Using 3D Slicer and Avizo, a total of 260 semilandmarks were collected from the decongested nasal passages of each individual. General Procrustes Analysis (GPA) was then used to align the semilandmark configurations of all 20 individuals and a Principal Component Analysis (PCA) was subsequently performed using the Geomorph package in R. Our results indicate PC1 (19.13%) largely contrasts CD individuals with positive PC1 scores (relatively narrower nasal passages) from HH individuals with negative PC1 scores (relatively wider nasal passages). These results generally conform to morphological expectations, suggesting a general concordance between skeletal and decongested soft-tissue nasal anatomy.

This study thus provides the impetus for future research investigating the relationship between ecogeographic variation in nasal soft-tissue anatomy and air-conditioning physiology.

ASSESSING ECOGEOGRAPHIC VARIATION IN THE NASAL PASSAGES UTILIZING 3D
SEMILANDMARKS

INTERNSHIP PRACTICUM REPORT

Presented to the Graduate Council of the
Graduate School of Biomedical Sciences at
University of North Texas
Health Science Center at Fort Worth
in Partial Fulfillment of the Requirements

For the Degree of

MASTER OF SCIENCE

By

Lyndee Ward, B.F.A, B.S.

Fort Worth, Texas

May 2021

ACKNOWLEDGEMENTS

To begin, I would like to thank my major professor, Dr. Scott Maddux, for his mentorship, guidance, and continuous support throughout the past year.

I would like to thank Elizabeth Thai for paving the way for the development of my project and her dedication and hard work that went into to providing the models of the decongested nasal passages I used in my practicum. I would like to extend thanks to Dr. Todd Yokley at Metropolitan State University of Denver and Dr. Heather Edgar and her colleagues at the University of New Mexico for providing access the CT scans for use in this practicum.

I would like to express my appreciation to the Graduate School of Biomedical Sciences at the University of North Texas Health Science Center for providing this opportunity to earn this graduate degree. Additionally, I would like to express my gratitude to the members of my graduate committee, Dr. Rachel Menegaz and Dr. Emma Handler, for their guidance and encouragement throughout this experience. I offer my gratitude to the members of the Center for Anatomical Sciences, Drs. Rustin Reeves, Rehana Lovely, Lauren Gonzales, Cara Fisher, Rex Mitchell, and my fellow student colleagues for all the assistance, advice, and support they provided to me. I would also like to thank my fellow members of The Maddux Lab, Alexa Kelly, Sarah Kim, Caroline Grace, and especially Elizabeth Thai for assistance with my project and for providing me with encouragement and inspiration.

Finally, I wish to express my appreciation for my husband and my family who has shown me relentless love, encouragement, and enthusiasm for pursuing my dreams and extended continuous support to help me achieve them. I could not have done this without their kindness and assistance. From the bottom of my heart, Thank you.

TABLE OF CONTENTS

ACKNOWLEDGMENTS	ii
LIST OF TABLES & FIGURES	v
LIST OF FIGURES	vi
CHAPTER I: INTRODUCTION	1
BACKGROUND & LITERATURE	2
Section 1 : Nasal Function	2
Section 2 : Nasal Anatomy	3
Section 3 : Air Conditioning in the Nasal Passages	5
Section 4 : Ecogeographic Variation in the Nasal Anatomy	7
Section 5 : Geometric Morphometrics	8
STUDY AIMS	9
CHAPTER II : MATERIALS & METHODS	11
Section 1: Sample Data and Characteristics	11
Section 2: 3D Model creation	12
Section 3: Landmarks	16
Section 4: Linear Measurements	18
Section 5: General Procrustes and Principal Component Analysis	20
Section 5: Statistical Analysis for Significance	21
CHAPTER III : RESULTS	23
Section 1 : Nasal passages	23
Section 2 : Craniofacial surface	28
Section 3 : Facial surface	31
Section 4 : Linear measurements	34
CHAPTER IV : DISCUSSION.....	36
CHAPTER V : CONCLUSIONS & SUMMARY.....	41
CHAPTER VI : INTERNSHIP EXPERIENCE	43
APPENDIX A.....	45
APPENDIX B.....	47

APPENDIX C.....	52
APPENDIX D.....	56
APPENDIX E.....	59
REFERENCES	68

LIST OF TABLES

TABLE 1: Sample size and characteristics	12
TABLE 2: Linear measurements and their descriptions.....	17
TABLE A: List of abbreviations.....	46
TABLE C1: List of landmarks for the nasal passages	54
TABLE C2: Landmarks for the craniofacial surface	55
TABLE C3: Landmarks for the facial surface	56
TABLE E1: PCA proportions of variance	60
TABLE E2: PCA scores for the nasal passage surface for all subjects	61
TABLE E3: Significance of PC scores for the nasal passage	61
TABLE E4: PCA scores for the craniofacial surface for all subjects	62
TABLE E5: Significance of PC scores for the craniofacial surface	62
TABLE E6: PCA scores for the facial surface for all subjects.....	63
TABLE E7: Significance of PC scores for the facial surface.....	63
TABLE E8: Results of centroid sizes for all subjects on all surfaces	64
TABLE E9: Significance of centroid size comparisons across groups	64
TABLE E10: Results of linear measurements for all subjects	65
TABLE E11: Significance of linear measurement comparisons across groups	66
TABLE E12: Post Hoc Dunn's Test z-values for significance between groups	67

LIST OF FIGURES

FIGURE 1: Illustration of nasal anatomy from a medial view	4
FIGURE 2: Illustration of the bony nasal cavity from an anterior view	5
FIGURE 3: Example of the decongested airway models	13
FIGURE 4: Example of the rendered 3D model of the nasal passages.....	14
FIGURE 5: Example of the rendered 3D model of the Craniofacial Surface.....	14
FIGURE 6: Example of the rendered 3D model of the facial surface.....	15
FIGURE 7: Depiction of the aligned surfaces and CT scans.....	16
FIGURE 8: Landmarks of the nasal passages.....	17
FIGURE 9: Landmarks of the Craniofacial Surface and facial surface	18
FIGURE 10: Example of method for linear measurements	19
FIGURE 11: Example of landmark configurations aligned with GPA	20
FIGURE 12: PCA plots for the nasal passages.....	23
FIGURE 13: Surface meshes of the PC1 extremes of the nasal passages.....	24
FIGURE 14: Surface meshes of the PC2 extremes of the nasal passages.....	25
FIGURE 15: Surface meshes of the PC3 extremes of the nasal passages.....	26
FIGURE 16: Box plots of the PC scores for the nasal passages	28
FIGURE 17: PCA plots of the craniofacial surface.....	29
FIGURE 18: Surface meshes of the PC2 extremes for craniofacial surface.....	30
FIGURE 19: Box plots of the PC scores for the craniofacial surface	31
FIGURE 20: PCA plots of the facial surface	32
FIGURE 21: Surface meshes of the PC1 extremes for facial surface	33
FIGURE 22: Box plots of the PC scores for the facial surface	34
FIGURE 23: Box plots for the linear distance measurements	35
FIGURE B1: Multiview example of the 3D model of the nasal passages	49
FIGURE B2: Example of the 3D craniofacial surface	49
FIGURE B3: Example of the 3D facial surface	50
FIGURE B4: Example of landmarks on the craniofacial model	50
FIGURE B5: Example of the type II landmarks on the 3D nasal passage model	51
FIGURE B6: Example of the type II landmarks on the medial meatus	51
FIGURE B6: Example of type II and type III landmarks on the nasal passage model	51
FIGURE B7: Example of landmarks placed on the facial model	52

CHAPTER I: INTRODUCTION

The following report was completed as a requirement for the Master of Science in Medical Sciences Anatomy Research Track program at the University of North Texas Health Science Center (UNTHSC). The study described here was performed between May 2020- May 2021, at UNTHSC in the Center for Anatomical Sciences and the Department of Physiology and Anatomy, under the supervision of Scott Maddux, PhD.

The human nose serves many functions, one of which is conditioning inspired air through filtration, warming, and humidification. Prior research has pointed to strong statistical relationships between geographically-patterned variation in nasal morphology and environmental/climatic variables such as temperature and humidity (Franciscus and Long, 1991; Noback et al., 2011; Yokley, 2009; Maddux et al., 2016). Additionally, more recent studies employing computational fluid dynamics (CFD) have evaluated how variation in nasal morphology influences airflow patterns within the nasal passage through (Mylinski, 2001; Dooly et al, 2008; Leong et al., 2010; Keustermans et al., 2020). However, virtually none of these airflow studies have 1) rigorously quantified variation in nasal passage size and shape, or 2 effectively controlled for the confounding effects of nasal congestion on the morphology of the soft-tissue nasal passages.

The purpose of this practicum was to develop a methodology for assessing shape variation in the soft tissue nasal passages using 3D modeling and semilandmark-based geometric morphometrics. This practicum builds off the previous work by Elizabeth Thai, MS, who

developed a methodology for digitally “decongesting” 3D models of the nasal passages for subsequent use in CFD analyses of nasal airflow (in conjunction with the Dennis Lab at the University of Texas at Arlington). This practicum continues this work by developing a process for accurately quantifying and analyzing differences in the complex 3D morphology of these nasal models. This practicum thus serves as a component of a larger study seeking to evaluate the functional relationships between ecogeographic variation in nasal morphology and airflow physiology.

BACKGROUND AND LITERATURE

Section 1: Nasal Functions

As the first portion of the respiratory tract, the nasal cavity performs many important physiological functions such as sensing airflow during respiration and housing sensory receptors for olfaction (Mygind and Dahl, 1998). The nasal cavity also performs immunological functions, filtering particulates and microbes as well as trapping and eliminating microscopic particulate and pathogens (Sahin-Yilmaz and Naclerio, 2010). The nasal cavity also notably performs the majority of the warming and humidification of inspired air to 37°C and 100% humidity before delivery to the alveoli of the lungs for gas exchange (Cole, 1982; Mygind and Dahl, 1998; Mylinski, 2001). Finally, the nasal cavity also plays an important role in thermoregulation, recapturing heat and moisture during exhalation in cooler environments and releasing excess heat in warmer environments (Walker and Wells Jr, 1961).

Section 2: Nasal Anatomy

The nasal passages form two bilateral hollow airspaces which start at the nares and continue posteriorly until ultimately merging into a single airspace at the nasopharynx (Mygind and Dahl, 1998). The upper respiratory tract is collectively comprised of many anatomical components, with the current project primarily focusing on two: the external nose and nasal cavity.

The external nose describes the complex anatomical structure that protrudes anteriorly from the face. Importantly, the external nose encapsulates the nasal vestibule, the first part of the nasal airways through which air travels during inhalation. The external nose is comprised of the paired nasal bones at the superior border, paired lateral cartilages that define the middle regions, and paired alar cartilages that shape the inferior aspects of the nose, including the nasal vestibule and nares. The external nose also houses multiple muscle attachments to help change the shape of the nares to meet respiratory needs. At the posterior boundary of the nasal vestibule is the internal nasal valve, a narrow region that serves to increase resistance, decrease airflow velocity, and redirect airflow as it enters the nasal cavity (Cole, 2000; Mylinski, 2001; Sahin-Yilmaz and Naclerio, 2010).

The external nose is covered in keratinized stratified squamous epithelium continuous with the face. The internal lining of the nasal vestibulum is covered with a stratified squamous epithelium that transitions to a pseudo-stratified columnar epithelium as it reaches the posterior most aspects of the nasal vestibulum (Mygind and Dahl, 1998; Sahin-Yilmaz and Naclerio, 2010).

The nasal cavity is the first internal portion of the upper respiratory tract and is completely encompassed by facial and cranial bones. The ethmoid forms most of the superior nasal cavity with contributions from the internal surfaces of the paired nasal bones anteriorly, and the sphenoid posteriorly. The maxilla forms the anterior nasal cavity floor and palatine contributes to the posterior floor of the nasal cavity. On Each side, the lateral nasal walls have contributions from the ethmoid, sphenoid, lacrimal, maxilla and the inferior nasal concha (turbinate) which projects from the lateral wall medially into the nasal cavity.

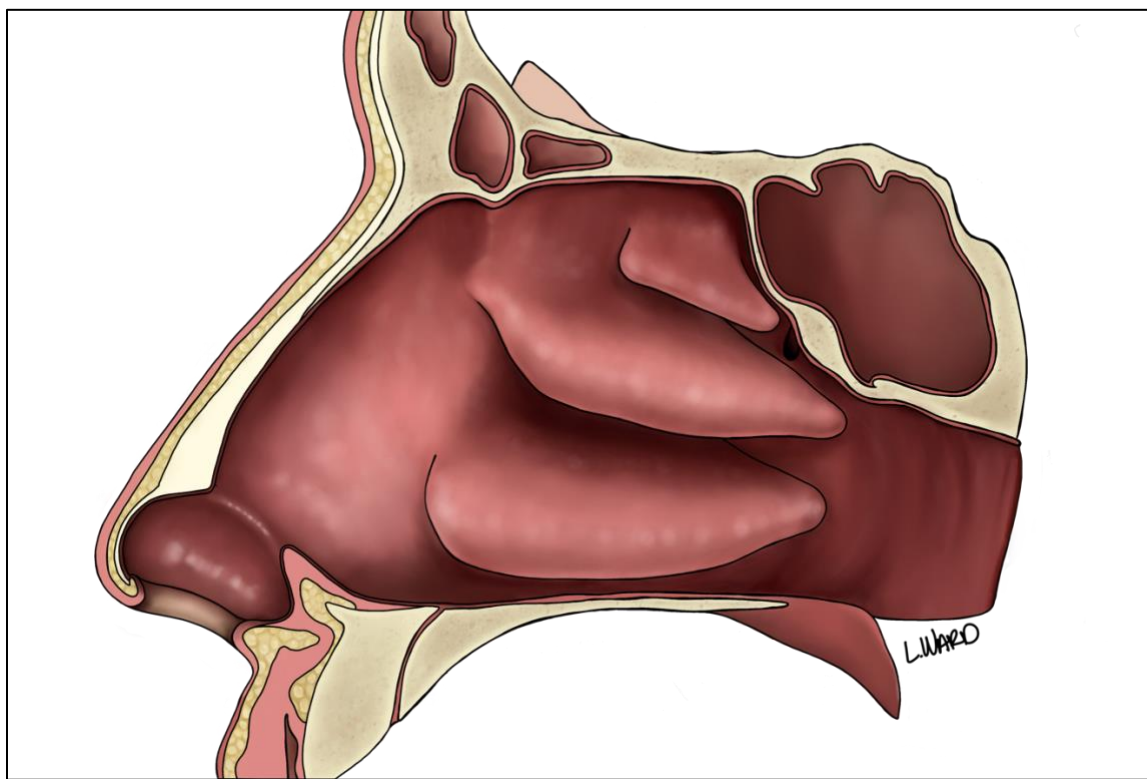


FIGURE 1: Medial view of the external nasal structures and nasal cavity.

The nasal septum comprised of both bone and cartilage divides the nasal cavity into left and right air chambers. There are three nasal turbinates in Each of these chambers, which arise from the lateral wall of the nasal cavity, projecting medially into the nasal passage (Mygind and Dahl, 1998; Sahin-Yilmaz and Naclerio, 2010). The inferior turbinate is the most inferior and

anterior of the turbinates, and is also usually the largest of the three. The middle turbinate lies superior and starts posteriorly to the inferior turbinate. The superior turbinate lies superior and starts posteriorly to the middle turbinate. Each turbinate creates a space beneath it called a meatus, with each meatus is named for its overlying turbinate: the superior meatus, middle meatus, and inferior meatus. In addition to these meatuses there is the common meatus which forms a medially-positioned air channel to which the superior, middle, and inferior meatuses connect (Mygind and Dahl, 1998; Sahin-Yilmaz and Naclerio, 2010).

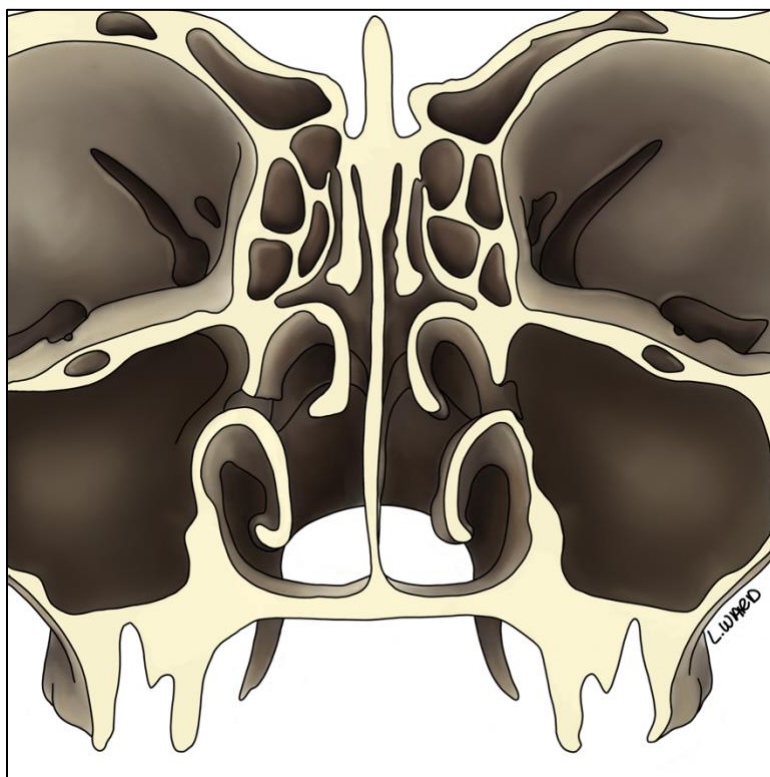


FIGURE 2: Illustration of a cross-section of the bony nasal cavity from an anterior view.

Section 3: Air conditioning in the nasal passages

To facilitate efficient gas exchange, inspired air must be adequately warmed and humidified before it reaches the lungs (Cole, 1982; Mygind and Dahl, 1998; Mylinski, 2013).

Importantly, the nose accounts for 90-95% of all inspiratory heat and moisture exchange, with only minor additional contributions from the pharynx and lower respiratory tract (Maddux et al., 2017). The pathway of inspired air first passes through the nares, followed by the vestibule and the internal nasal valve. Upon entering the nasal cavity, the flow of air is distributed across the four meatuses (i.e., common, inferior, middle, and superior) and then passes through the choanal openings to enter the pharynx and ultimately the larynx and lower respiratory track (Cole, 2000; Mylinski, 2001).

Nasal air-conditioning predominantly occurs within the nasal cavity (Cole, 1982; Maddux et al., 2017). Inspired air is directed to the nasal cavity after passing through the nasal vestibulum and internal nasal valve. These structures serve to adjust the direction, velocity, and distribution of the incoming airstream across the meatuses within the nasal cavity (Doorly, et al., 2008; Leong et al., 2010). As inspired air flows through the meatuses, these smaller air channels facilitate contact with the serous coated mucosa of the surrounding structures, warming the air via convection and humidifying the air through evaporation. While this mucosa-air interaction during inspiration serves to adequately warm and humidify inspired air, it also leaves the post-inspiratory nasal mucosa cooler and drier (Walker and Wells Jr, 1961; Cole, 1982; Mlynki, 2013). However, upon expiration, warm-wet air returning from the lungs once again passes through the nasal cavity, from which the cool-dry nasal mucosa recaptures heat and moisture via convection and condensation respectively. This recapture of heat and moisture prepares the nasal mucosa for the next bout of inspiratory conditioning, helping to conserve energy and preventing desiccation of the airway mucosa (Walker and Wells Jr, 1961; Cole, 1982).

The two sides of the nasal cavity participate in the nasal cycle where one side performs the bulk of the conditioning while the other side rests and recuperates moisture. The active half

of the cavity displays decongested nasal mucosa reducing the surface area of the mucosal surface and increasing the volume of the airway. The resting side of the nasal cavity increased mucosal congestion resulting in increased surface area of the mucosal surface and a decreased volume of the airways (Onerci, 2013; Sahin-Yilmaz and Naclerio, 2010).

Section 4: Ecogeographic variation in nasal morphology

Prior research has established correlations between nasal morphology and the external environment, namely temperature and humidity (Walker and Wells Jr, 1961). Relatively taller and narrower nasal cavities have been shown to be associated with cold and dry environments, whereas relatively shorter and wider nasal cavities have been associated with warmer more humid environments (Franciscus and Long, 1991; Noback et al., 2011; Yokley, 2009; Maddux et al., 2016). It has also been noted that more projecting external noses are associated with colder and drier environments, while flatter external noses are associated with warmer more humid environments (Carey and Steegman, 1981).

These associations support assertions that climatic pressures have evolutionarily influenced geographically-patterned variation in human nasal morphology (Franciscus and Long, 1991; Noback et al., 2011). In cold-dry environments, a taller and narrower nasal cavity increases the surface area of the nasal mucosa relative to the volume of air capable of filling the nasal cavity. This higher surface area-to-volume (SA/V) ratio provides more contact between the nasal mucosa and inspired air, facilitating heat and moisture exchange. These characteristics thus ensure that cold-dry inspired air has sufficient contact with the mucosa to achieve the required 37°C and humidification to 100% saturated with water vapor. Additionally, this increased SA/V ratio facilitates more contact for heat and water recapture on exhalation which helps to re-heat

and hydrate the nasal mucosa before the next bout of inspiration. A shorter and wider nose on the other hand reduces the surface area of the nasal mucosa and increases the volume of air within the nasal cavity, which results in less contact between air and the nasal mucosa. This is appropriate as in warmer and more humid environments air does not require the same level of warming and humidification as a colder and dry environment (Franciscus and Long, 1991; Noback et al., 2011; Yokley, 2009; Maddux et al., 2016, Zaidi et al., 2017)

Section 5: Geometric Morphometrics

Geometric morphometrics a collection of procedures for statistical analysis of variation in shapes based upon configurations of homologous landmarks that controls for differences in size, orientation, and spatial location (Bookstein, 2004; Zelditch et al., 2004; McKeown and Schmidt, 2013). Geometric morphometrics is a set of procedures developed off the backbone of traditional morphometric analysis. Traditional morphometrics uses linear distance measurements to describe the shape of a structure, however; these measurements do not provide information on the spatial relationships between the measurements and are limited in the information of shape variation that can be extracted with these methods (Zelditch et al., 2004). Geometric morphometrics is based on landmarks, points representing a homologous or defined location on a structure, which are assigned to a set of cartesian coordinates or a triangular plane of a 2D or 3D surface. This allows for the extraction of information about distance and the relationships between multiple landmarks, providing more robust information on shape or spatial form (Zelditch et al., 2004).

In geometric morphometrics there are different types of landmarks that can be used in analysis. The first are Type1 Landmarks, described by Fred Bookstein as homologous locations on a structure that represent distinct intersections or characteristics (Bookstein, 2004). Cranial

sutures, particularly the intersections of them, are good example for a Type 1 landmark, these are often employed in investigations on craniofacial morphology. Type 2 Landmarks are landmarks that can be defined and reliably replicated, generally these are defined in terms of extremes of a surface of a structure (McKeown and Schmidt, 2013; Gunz and Mitteroecker, 2012). For example, “the most anterior point of the nasal bones”, or “the point of maximum curvature along the external nose.” Type 3 Landmarks are dependent upon other defined landmarks in a configuration to describe and replicate their position (Bookstein, 2004). Semi-landmarks are a type 3 landmark, whose position in a configuration depends on fixed landmarks and that are optimized through landmark sliding to become equidistant from each other. Semi-landmarks open the door for thoughtful consideration of curves and entire surfaces where replicability of landmark placement would be difficult and unreliable. Semi-landmarks can be initially placed manually and later optimized through the use of algorithms. Alternatively, semi-landmarks can be generated through an algorithm based on the creation of a surface patch in an appropriate software program which then reiterates the position of these landmarks until they are at an optimal position. (Bookstein 2004, McKeown and Schmidt, 2013, Gunz and Mitteroecker, 2012).

SPECIFIC AIMS AND OBJECTIVES

Aim: To develop a replicable process to accurately quantify and evaluate morphological variation in soft tissue nasal passages utilizing 3D models for subsequent use in computational fluid dynamics analyses.

Objective 1: *Assess the ability of the newly developed method to detect ecogeographic difference in overall height, breadth, and length dimensions in the decongested nasal passages.*

Using linear measurements, Yokely (2009) has previously shown that the individuals comprising our cold-dry descended group generally exhibit taller, narrower, and longer nasal passages than individuals in our hot-humid descended sample. It is thus predicted that the newly developed 3D method will identify the same morphological pattern.

Objective 2: *Evaluate the capacity of the new methodology to detect morphological differences in meatus (inferior, middle, superior, and common meatuses) morphology across decongested nasal passages.* Employing linear measurements, Marks et al., (2019) have demonstrated that individuals ancestrally derived from cold-dry environments typically exhibit taller, narrower, and longer meatus dimensions than individuals derived from hot-humid environments. It is thus predicted that the new method will identify the same pattern of 3D morphological variation in the current sample.

Objective 3: *Determine the efficacy of the new 3D method in detecting ecogeographic variation in external nasal anatomy.* Previous research (Carey and Steegmann, 1981; Zaidi et al., 2017) employing linear measurements have demonstrated a tendency for individuals derived from cold-dry environments to possess narrower and more projecting soft-tissue external noses compared to individuals from hot-humid environments. Accordingly, it is predicted that the new 3D method will also show this morphological pattern.

CHAPTER 2: MATERIALS AND METHODS

Section 1: Sample

Table 1 provides summary information regarding the sample employed in this study. This sample consists of 20 computed tomography (CT) scans from adult heads collected from the larger datasets of Yokley (2009) and the New Mexico Decedent Database (Edgar et al., 2020). Subjects allocated from the Yokley collection ($n = 18$) were obtained from the Otolaryngology or Head and Neck Surgery Clinic at the University of North Carolina at Chapel Hill Hospital and excludes individuals with histories of nasal surgery, abnormal nasal anatomy, or excessive inflammation of the nasal mucosa. Subjects collected from the New Mexico Decedents Database ($n= 2$) were screened and similar exclusions were applied for these subjects. Scans from the Yokley collection have the following parameters: (1) acquisition matrix of 512 x 512 pixels, (2) pixel size of 0.3 x 0.3 mm, and (3) voxel depth of 0.7 mm. Scans from the New Mexico Decedent Database had the following parameters: (1) acquisition matrix of 512 x 512 pixels, (2) pixel size of 0.51 x 0.51mm, and (3) voxel depth of 0.5 mm. The sample of 20 comprises 9 African American subjects representing ancestral adaptation to a hot-humid environment and 11 European American subjects representing ancestral adaptation to a cold-dry environment. The sample includes 9 male and 11 female subjects. The sample, portioned by sex and descent is composed by the following: 5 hot-humid females, 4 hot-humid males, 6 cold-dry females and 5 cold-dry males.

TABLE 1: Sample information

Subject	Database	Descent	Sex	Age
Y002	Yokley	CD	M	54
Y003	Yokley	CD	F	37
Y004	Yokley	HH	F	57
Y005	Yokley	CD	F	52
Y012	Yokley	HH	F	53
Y013	Yokley	HH	M	52
Y015	Yokley	HH	M	61
Y023	Yokley	CD	M	42
Y045	Yokley	CD	F	37
Y055	Yokley	CD	M	40
Y056	Yokley	HH	F	61
Y071	Yokley	CD	F	60
Y083	Yokley	CD	M	46
Y087	Yokley	CD	M	22
Y093	Yokley	CD	F	60
Y101	Yokley	CD	F	53
Y105	Yokley	HH	F	49
Y109	Yokley	HH	F	49
NM304	NMDD	HH	M	NA
NM030	NMDD	HH	M	NA

Section 2: 3D Model Creation

The 3D models of the nasal passages were generated following the procedures developed by Elizabeth Thai in her 2020 Master of Medical Science-Anatomy Internship Practicum under the guidance and mentorship of Scott Maddux, Ph.D. The 3D models generated represent the maximum airspace within the nasal passages after controlling for soft tissue nasal congestion. The nasal passage models represent the negative space in the nasal passages. This positive 3D rendering of the negative airspace is a requirement for subsequent CFD analysis.

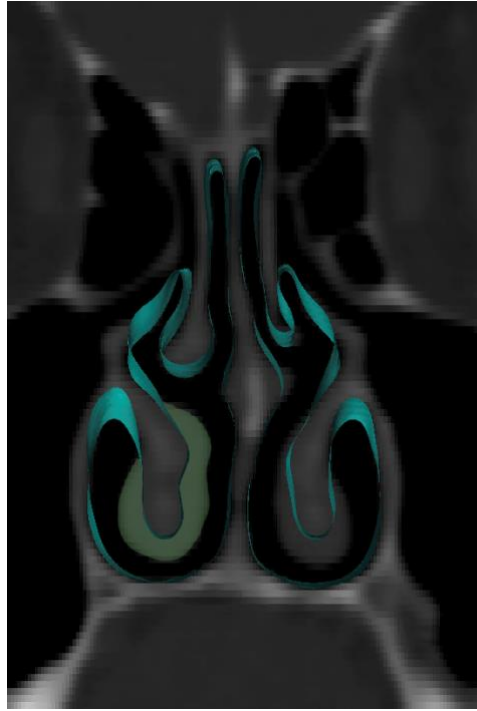


FIGURE 3: Visualization of the nasal passages demonstrating correction for mucosal congestion. The congested mucosa is highlighted in green on the left side of the image (i.e., right nasal passage), while the right side of image shows the normal appearance of nasal mucosa on a CT slice. The surface area of mucosa following digital decongestion is highlighted in blue.

The artificially decongested model of the 3D nasal cavity was generated in 3D Slicer using automated thresholding, masking, and manual CT segmentation to isolate the bony structures of the nasal anatomy. A new CT segmentation layer was generated, and an inverse operation was applied thereby selecting the regions of maximum airspace in the nasal cavity. This segmented region was then rendered as a 3D model and saved as a Standard Tessellation Language (STL) file (Thai, 2020). The 3D models were then imported into ThermoFisher Scientific Avizo 8 software (Thermo Fisher Scientific, Waltham, MA, US) and the 3D mesh was edited to isolate the nasal passages from the surrounding airspace and the once again saved as an STL file.

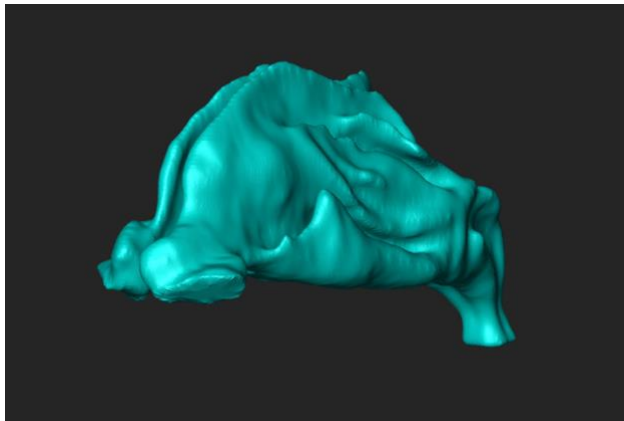


FIGURE 4: Example of a completed 3D model of the decongested nasal passage from an anterolateral view.

The 3D models of craniofacial bones were generated using ThermoFisher Scientific Avizo 8 software (Thermo Fisher Scientific, Waltham, MA, US). The series of CT DICOM images for Each subject were loaded into Avizo and an orthoview frame was applied to the data set for viewing. An isosurface display module was attached to the dataset and the threshold level changed to isolate the grey values indicative of bone (generally the isosurface threshold was set between 200 and 300). Once the Isosurface is generated the surface was extracted, creating a new data object which was then exported and saved as an STL file.

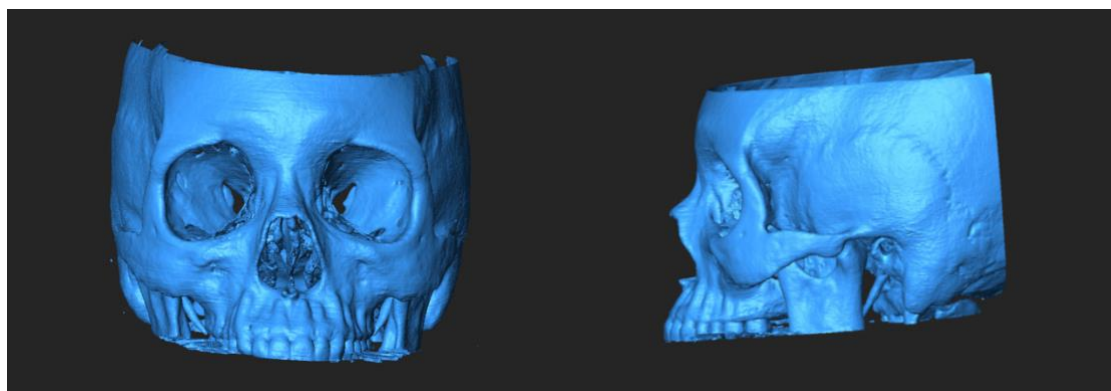


FIGURE 5: Example of the 3D model of the Craniofacial Surface from an anterior (left) and lateral perspective (right).

The 3D models of subject facial surface features were similarly generated using Avizo 8 software. The series of CT DICOM images for a subject were loaded into Avizo and an orthoview frame applied to the data set for viewing. An isosurface display module was then attached to the dataset and the threshold level is changed to isolate the grey values encompassing all soft tissues (generally the isosurface threshold was set between -600 and -400). Once the Isosurface was generated, the surface was extracted creating a new data object, which was exported and saved as an STL file.

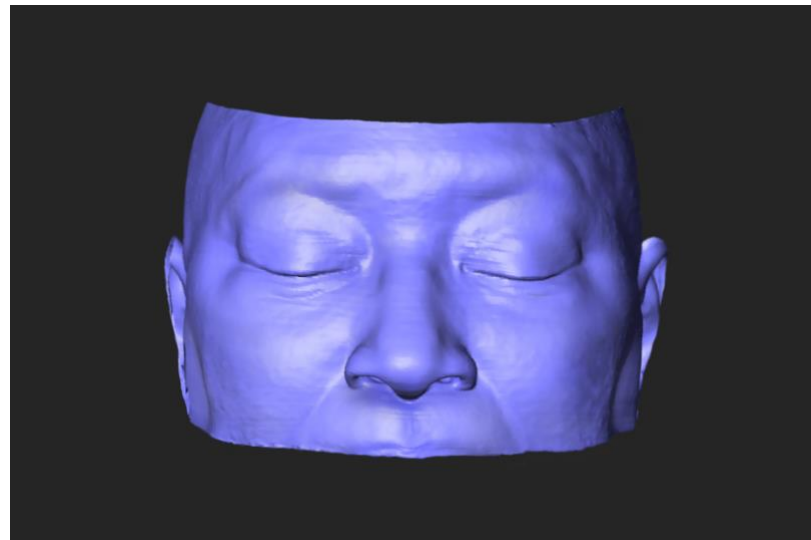


FIGURE 6: Example of the 3D model of the facial surface viewed from an anterior perspective.

The 3D models of the nasal passage, cranium, and the CT scan data for Each individual subject were loaded into the project space in Avizo for alignment. Employing the cranium model in the transformation editor, the model was transformed to the Frankfort Horizontal Plane. The transformation was then copied and applied to both the nasal passage model and the CT data. The CT data object was then resampled to conform to the applied transformations and saved as a new data object. The transformed and aligned 3D models were then saved.

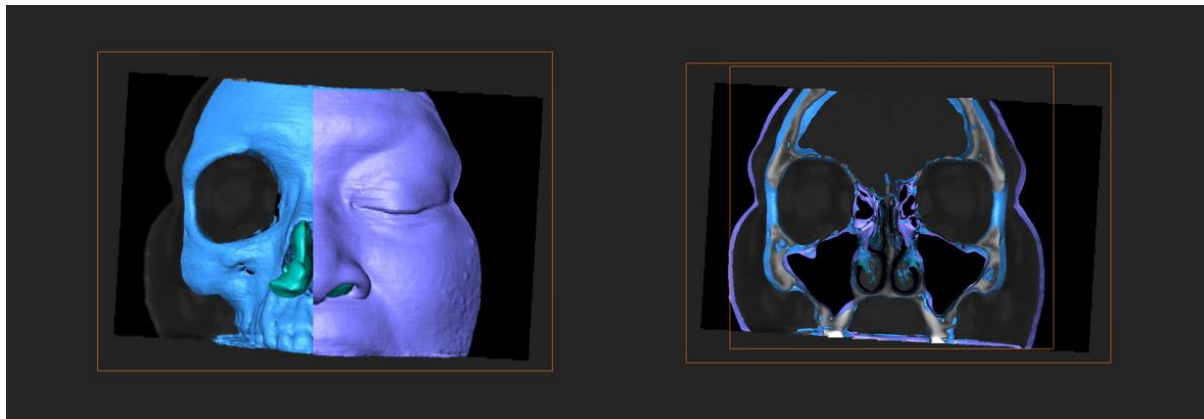


FIGURE 7: Examples of the alignment of facial surface (purple), Craniofacial Surface (blue), decongested nasal passage (green) and the resampled CT scan (gray) for an individual subject in Aviso 8. The left image shows an anterior view of this alignment with the facial surface hemisected with a clipping plane to visualize the Craniofacial Surface, nasal passages and resampled CT scan. The right image depicts all three models with an overlying clipping plane and an intersecting orthoslice.

Section 3: Landmarks

All landmarks were placed using the Avizo 8 software package. The landmark data were then exported to Microsoft excel for formatting, and subsequently loaded in R for statistical analysis.

A total of 262 landmarks, outlined in Table 2, were placed on Each 3D nasal model. There were 42 type II landmarks placed at definable positions on the nasal passages to serve as anchoring points for semilandmarks. A total of 25 semi-landmarks were placed along the superior border of the nasal cavity, 25 semi-landmarks were placed along the inferior border of the nasal passage, and 20 semi-landmarks were placed along the superior ridge of Each meatus

(superior, middle, and inferior) bilaterally. The landmark placement and configuration for the nasal cavity were based on a prior study by Bastir and colleagues (2019).

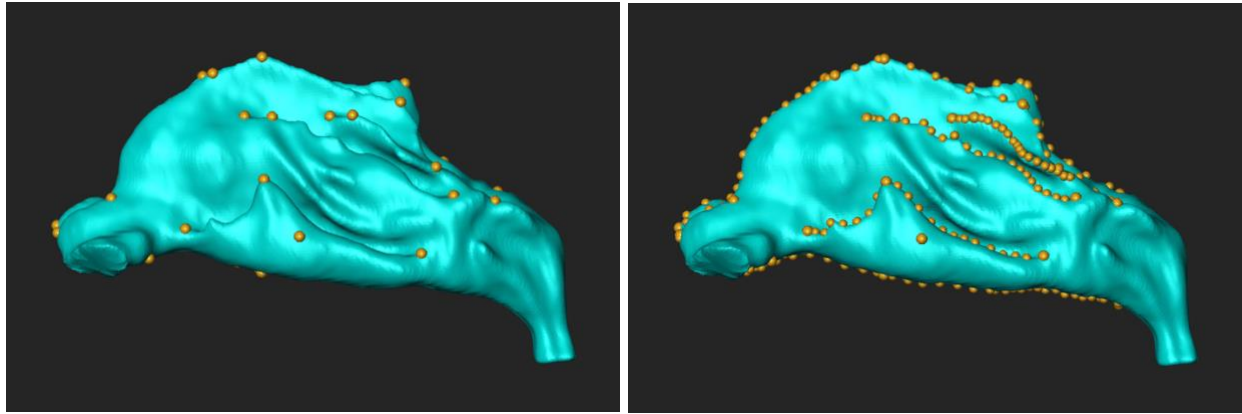


FIGURE 8: Examples of the landmarking procedures on a lateral view of the 3D nasal passages, where type II landmarks are visualized on the left and both Type II and Type III (semilandmarks) are shown on the right.

Landmarks were placed on a 3D surface rendering of the craniofacial bones of Each subject. The landmarks selected, detailed in Table 1, are craniometric points, commonly employed in prior studies of anatomical nasal variation that describe the nasal morphology and its limiting bony boundaries. Finally, landmarks were placed on the facial surface model at locations that describe the external nasal structures. By employing skeletal landmarks along with the semilandmarks on the nasal cavity and facial surface a comprehensive configuration of landmarks is generated that represents all the anatomical structures that impact nasal morphology. This process allows for a more robust analysis of nasal morphology considering both size and shape variation and allows for comparison between our results and the results of prior research.

Landmark configurations consisting of the type 1 and type 2 landmarks and semilandmarks for each tissue layer (nasal passages, craniofacial bones, and facial surface) were compiled in excel and input to the Morphologika file format in Notepad and saved by layer as .txt files.

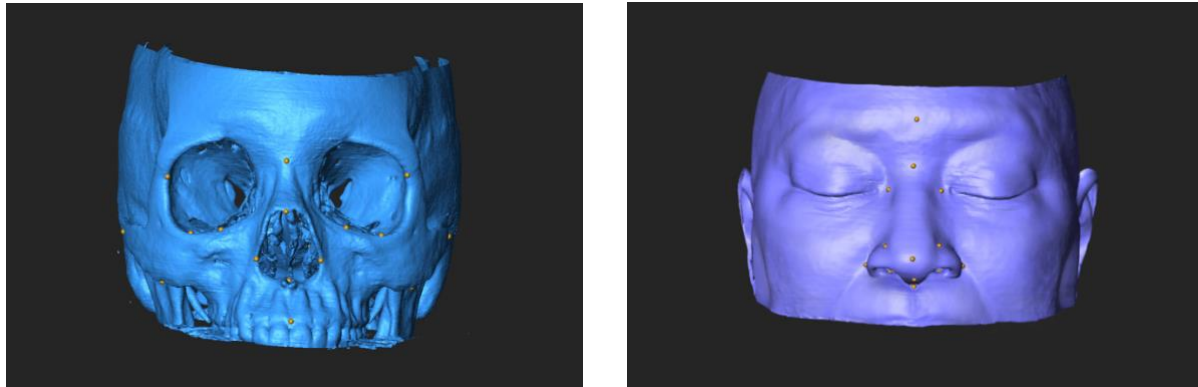


FIGURE 9: Example of the landmarks from an anterior view on the Craniofacial Surface (left) and facial surface (right).

Section 4: Linear Measurements

Linear distances outlined in table 2, were obtained utilizing Avizo 8 Software. A clipping plane and an orthoslice were attached to the craniofacial 3D model, the orthoslice plane was positioned to intersect the landmarks representing the ends of the linear measurement. The clipping plane was placed approximately one slice in front of the orthoslice and the view toggle was activated to hide faces of the 3D surface positioned in front of the clipping plane. The measurement tool was then used to place a straight line on the orthoslice between the two landmarks. The lines representing the linear distances were viewed from a sagittal perspective to ensure they set in one plane.

TABLE 2: Linear measurements and their descriptions

Linear Measurements	
External Nasal Height	Length of line from the nasion to the nasospinale
Nasion to Prosthion	Length of line from the nasion to the prosthion
Nasal Alare Breadth	Length of the line from the points of the left and right nasal alare
Internal Nasal Height	Length of the line from the ethmoidal to the nasal floor
Inferior Nasal Fossa Breadth	Length of the line between the left and right inferior nasal fossa points
Choanal Height	Length of the line from the staphylion to the midline between the choanal apexes.
Choanal Breadth	Length of the line between the left and right choanal alare points.

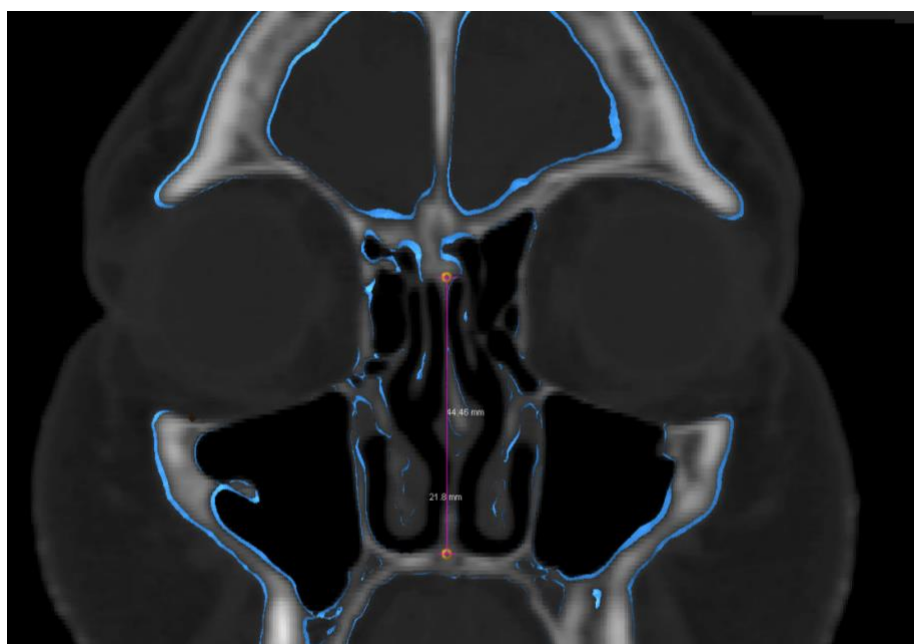


FIGURE 10: Example of the procedures for taking linear measurements in Avizo. The Craniofacial Surface is shown with an overlying clipping plane just anterior to the intersecting orthoslice. The measurement line (pink) is placed on top of the orthoslice to connect the two landmarks (yellow) resulting in a measurement line that rests in one plane.

Section 5: General Procrustes Analysis and Principal Component Analysis

Statistical Analyses were performed utilizing the geomorph package in R (Adams et al., 2021) and NCSS (NCSS, 2016).

The landmark configuration for the nasal passages of each individual was compiled into a Morphologika file format and imported to R. The data was checked for missing data and missing values were estimated. A data table of the semilandmarks identifiers and sliding direction was imported into R. A Generalized Procrustes Analysis (GPA) was then performed to resize, rotate, and reorient all the individual landmark configurations to one consistent coordinate system and obtain centroid sizes for all individual landmark configurations. The mean shape of the landmark configurations was then determined.

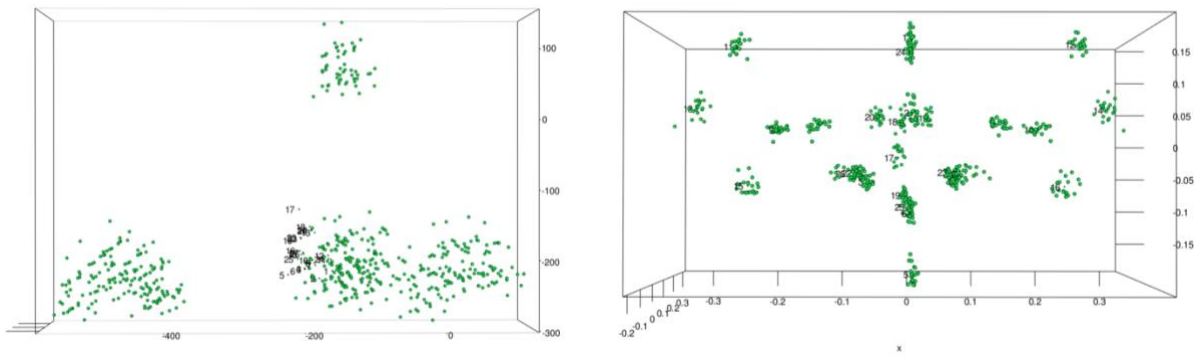


FIGURE 11: Example of Landmark configurations of the Craniofacial Surface for all subjects before GPA (left) and after GPA (right).

After the landmark configurations were standardized to a consistent coordinate system with the GPA, a Principal Component Analysis (PCA) was conducted. Principal Component values for each subject were plotted to visualize and a table of each subject's PC scores was generated and exported for statistical analysis. The shapes of the PC minimums (extreme negative scores) and maximums (extreme positive scores) were visualized utilizing surface mesh warps. To obtain the surface mesh warps, the subject with a landmark configuration that most

closely approximated the mean configuration was identified. A table of the landmark coordinates belonging to the mean subject were isolated in a separate table in R. The 3D model of the nasal passages, saved as an American Standard Code Information Interchange Polygon File Format (ASCII PLY) file format, for the mean subject was imported to R. The mean subject's 3D model, landmarks, and the mean shape of the complete data set were used to create a 3D mesh of the mean shape. This mesh was then warped to match the landmark configurations of the PC extremes. The 3D meshes of the PC minimums and maximums were exported from R as Polygon File Format (PLY) files. These were then visualized in Blender and Adobe Dimension for reporting differences in appearance and rendering models in 2D figures for this report.

Section 6: Statistical Analysis for Significance

All statistical analysis for significance was performed utilizing the NCSS 11 software (NCSS, LLC, 2016). Means of centroid sizes of the nasal passage, Craniofacial Surface, and facial landmark configurations, linear measurements of the Craniofacial Surface, and principal component scores accounting for greater than 10% of the variance of the nasal passage, Craniofacial Surface, and facial landmark configurations were tested significant differences between CD and HH groups. Though it is a general practice to perform a Multivariate Analysis of Variance (MANOVA) to assess statistical significance across multiple variables (e.g. PC scores) simultaneously, due to the small sample sizes ($n= 4$) and unequal variances of present in certain sub-samples, this could not be performed. Instead, the nonparametric Kruskal-Wallis test (alpha= 0.05) was employed to assess for significant differences in variables across our smaller sub-samples based on our two factors (ancestry and sex): HH females, HH males, CD females,

and CD males. Dunn's post hoc tests were then performed to identify which particular groups the significant differences existed between.

CHAPTER III : RESULTS

Section 1: Nasal Passages

Principal Component 1 (PC1) accounted for 19.13% of the variation and contrasts variation related to relative nasal passage length and width. The warped surface mesh of the configuration for the PC1 maximum is characterized by a relatively long and narrow nasal passages. More specifically, the anterior cavum is elongated (anteroposterior) for representatives of the PC1 maximum and wider across the turbinate chamber. This is contrasted by the shape of the PC1 minimum which reflects relatively short (anteroposterior) anterior cavum and wide turbinate chamber. The plots of the PC1 scores shows a tendency for HH individuals to plot toward the PC1 minimum (shorter/wider) whereas, CD individuals tend to score towards the PC1 maximum (taller/narrower).

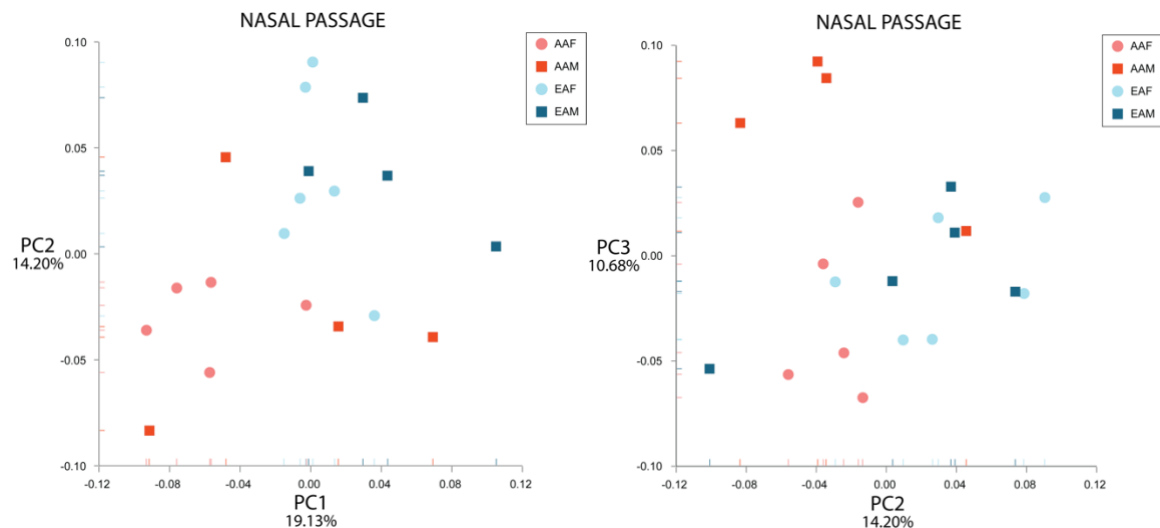


FIGURE 12: PCA plots for the nasal passages, On the left PC1 is plotted against PC2, Right shows PC2 plotted against PC3

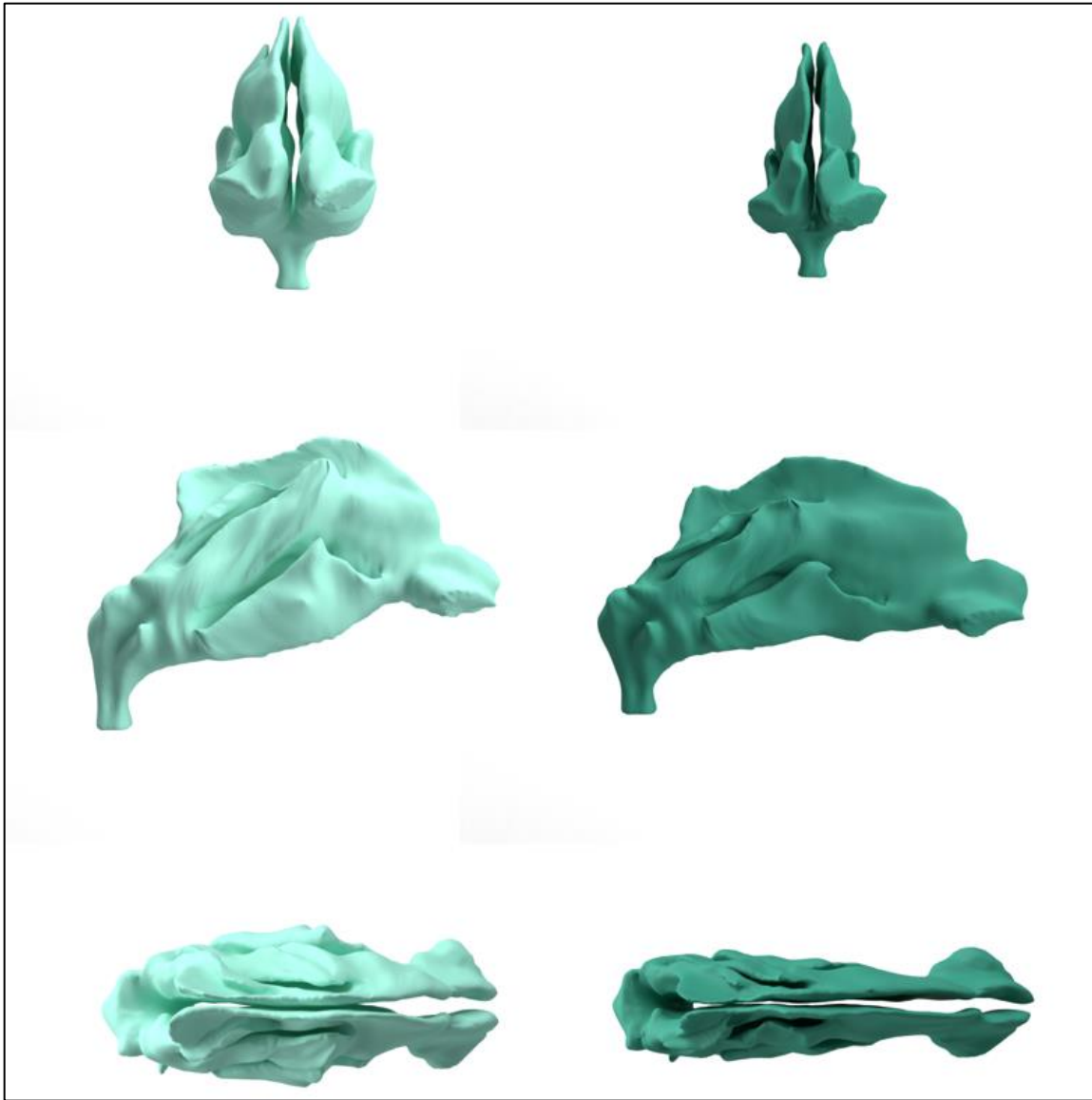


FIGURE 13: Rendered surface meshes representing the shape contrasts at PC1 minimum (left) and PC1 maximum (right). Top shows the anterior view, middle shows a lateral view, and bottom shows a superior view of the models.

Principal Component 2 (PC2) accounted for 14.20% of the variation in the nasal passage morphology and contrasts relative height and width dynamics. Representatives at the PC2 minimum have nasal passages that are relatively shorter in height and broader. This dynamic is more specifically seen across the inferior and middle meatuses. The PC2 maximum conversely

appears relatively narrow and tall overall, with especially tall and narrow middle meatuses and inferior meatuses. The plot of PC2 scores clusters CD individuals towards the maximum and HH individuals towards the minimum values.

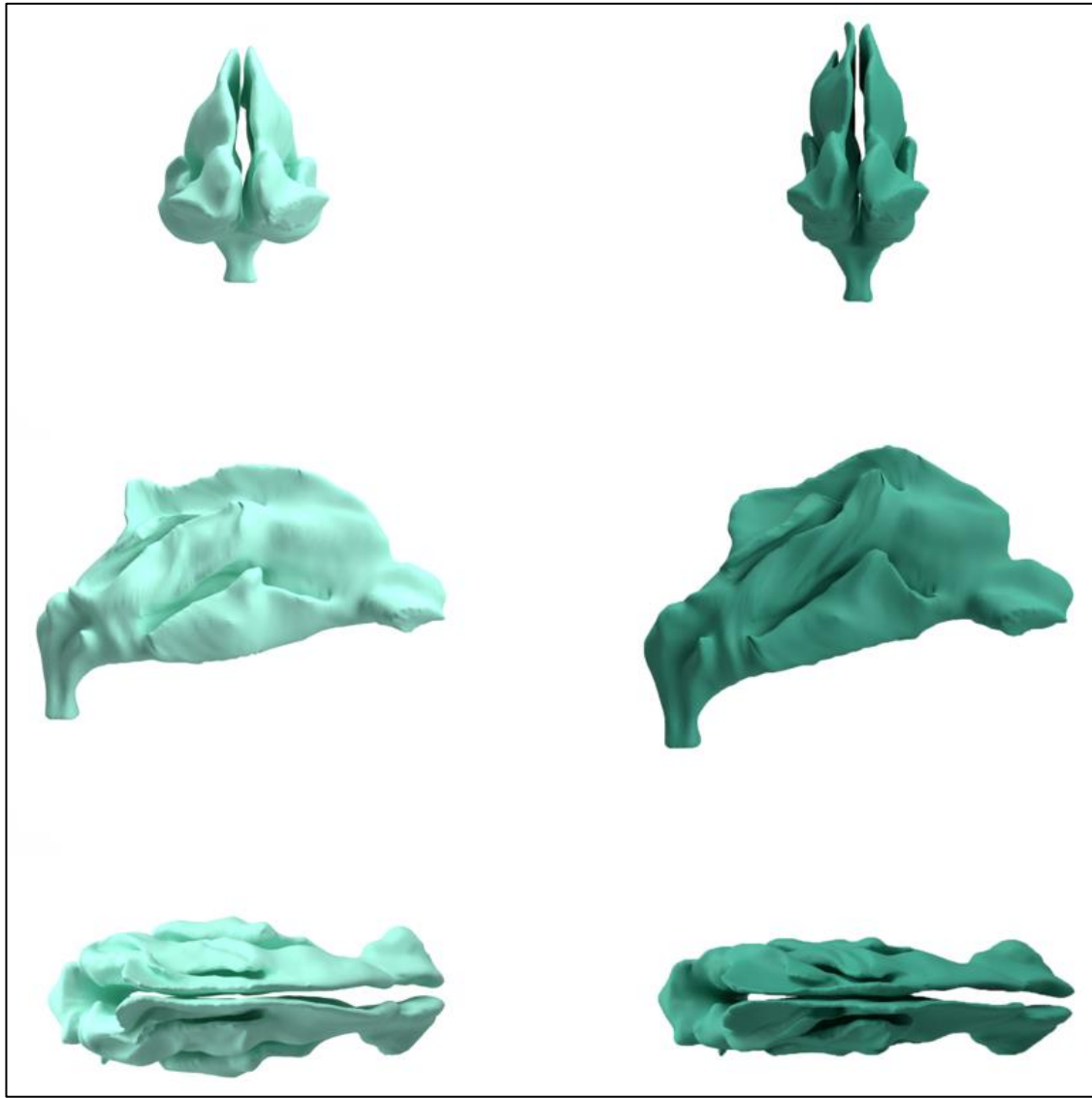


Figure 14: Rendered surface meshes representing the shape contrasts at PC2 minimum (left) and PC2 maximum (right). Top shows the anterior view, middle shows a lateral view and bottom shows a superior view of the models.

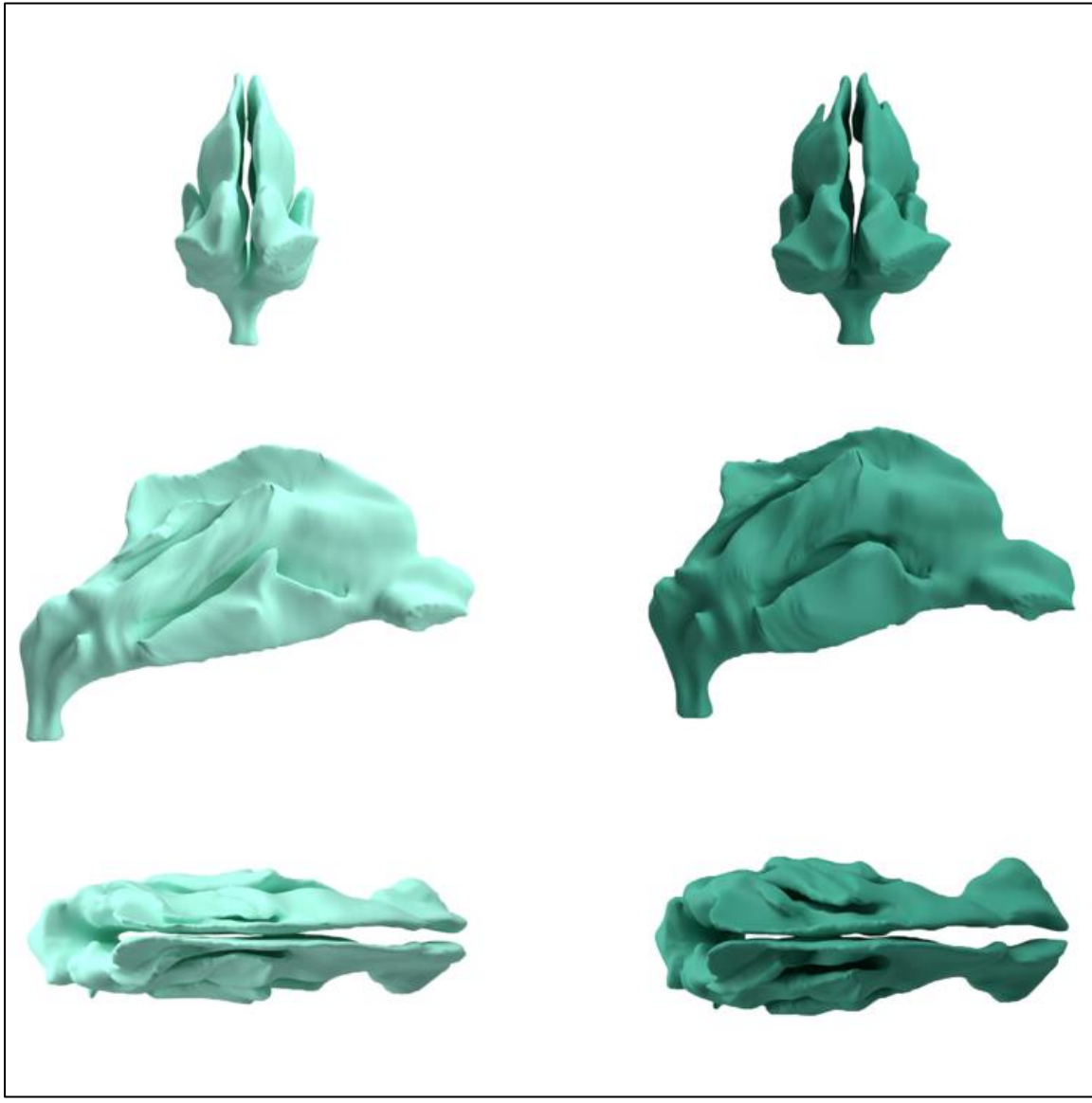


FIGURE 15: Rendered surface meshes representing the shape contrasts at the PC3 minimum (left) and PC3 maximum (right). Top shows the anterior view, middle shows a lateral view and bottom shows a superior view of the models.

Principal Component 3 (PC3) accounted for 10.68% of the variation in the nasal passages and contrasts length and breadth dynamics. The shape of the PC3 minimum appears relatively longer, particularly in the posterior nasal cavity approaching the choana and the nasal vestibulum, and narrower, specifically across the nares and nasal vestibulum. Representatives at

the PC3 maximum have a shorter (anteroposterior) and broader posterior nasal cavity and nasal vestibulum. The plot of PC3 scores shows HH males at the maximum, and HH females toward the minimum with CD males and females falling between the two.

Significance testing for centroid sizes of the nasal passages returned significant ($\chi^2 = 10.38$, **p=0.016**) between the four groups. The following Dunn's test revealed significant differences between HHF and CDM ($z = 2.25$, **p < 0.05**) and CDF and CDM ($z = 3.06$, **p < 0.05**). PC1 scores were also significant ($\chi^2 = 9.99$ **p=0.019**) with the only difference being between HHF and CDM ($z = 3.15$, **p < 0.05**). PC2 scores exhibited no significant differences between groups ($\chi^2 = 5.68$ **p=0.129**). PC3 scores displayed significant differences between groups ($\chi^2 = 7.98$ **p=0.04**) attributable to pair-wise difference between HHF and HHM ($z = 2.75$, **p < 0.05**) as well as between HHM and CDF ($z = 2.09$, **p < 0.05**).

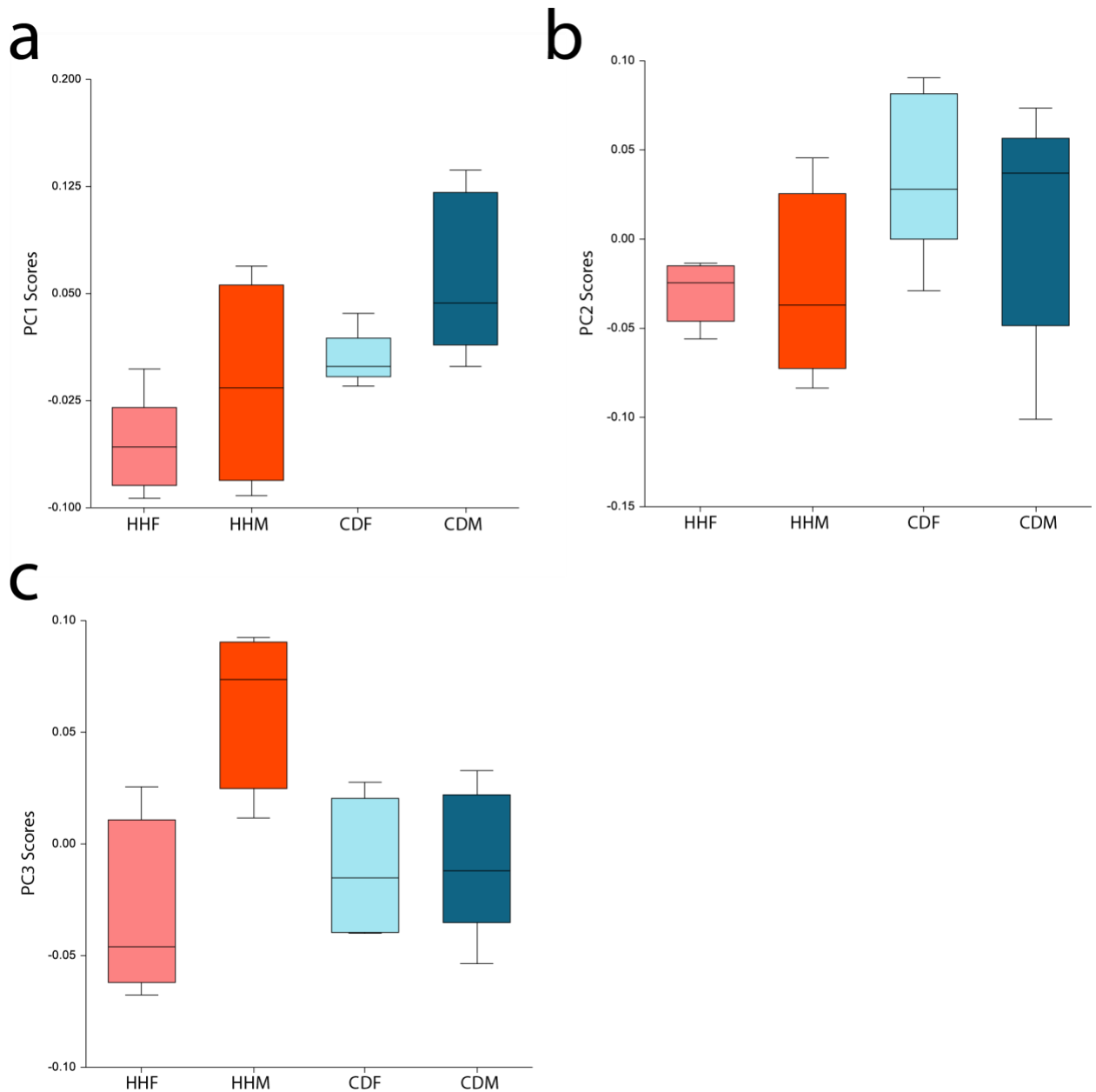


FIGURE 16: Box plots of the nasal passage surface PC1 scores by group (a), PC2 scores by group (b), and PC3 scores by group (c).

Section 2: Craniofacial Surface

For the Craniofacial Surface PC1 accounted for 21.93% of variation, PC2 accounted for 15.84% of variation, PC3 accounted for 12.26% of variation, and PC4 accounted for 10.92%.

Plots of PC1, PC3, and PC4 show all individuals dispersed with no clear clusters by descent or sex, while PC2 shows CD individuals clustered toward the maximum value and HH individuals clustered towards the minimum value. PC2 contrasts relative height and breadth of the craniofacial bones comprising the nasal cavity. Individuals at the PC2 maximum have a taller and narrower nasal aperture and nasal cavity. Additionally, subjects at the PC2 maximum show greater protrusion of the nasal bones. Conversely representatives at the PC2 minimum have a shorter and wider nasal apertures and nasal cavities as well as nasal bones with less protrusion.

Evaluation of centroid sizes of the Craniofacial Surface were nonsignificant between groups ($\chi^2 = 6.17$ p=0.10). Differences in median scores for PC1 ($\chi^2 = 2.58$ p=0.46), PC3 ($\chi^2 = 1.05$ p=0.78), and PC4 ($\chi^2 = 3.51$ p=0.32) did not reach significance between any group comparisons. The PC2 scores were significant ($\chi^2 = 14.52$ p=**0.002**) with significant pair-wise differences occurring between HHF and CDF (z=2.39, p < **0.05**), HHF and CDM (z=2.78, p < **0.05**), CDF and HHM (z=2.60, p < **0.05**), and HHM and CDM (z=2.96, p < **0.05**).

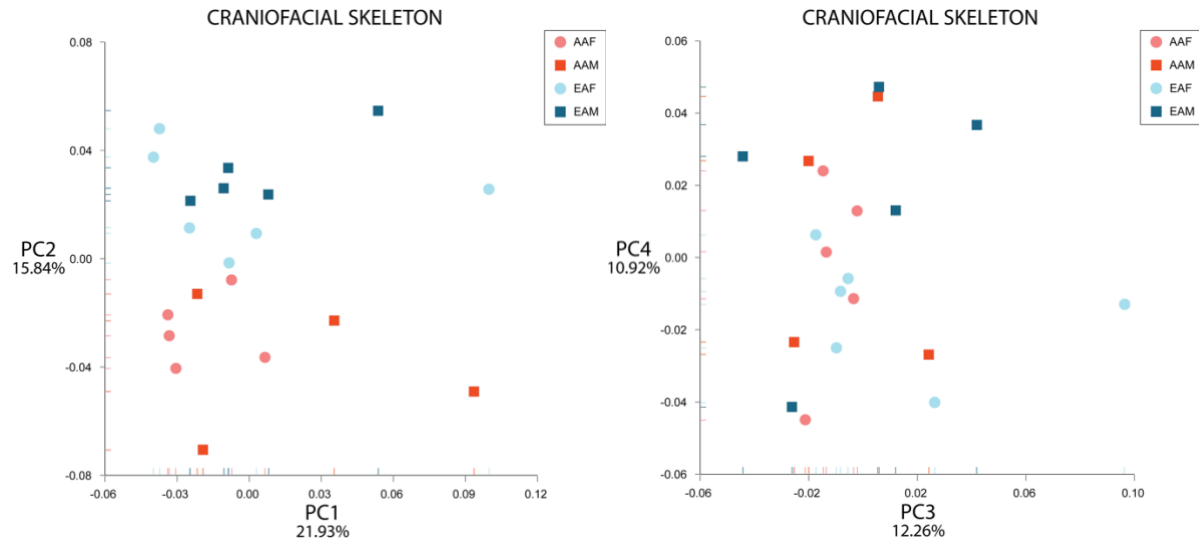


FIGURE 17: PCA plots for the Craniofacial Surface, PC1 against PC2 (left) and PC3 against PC4 (right).

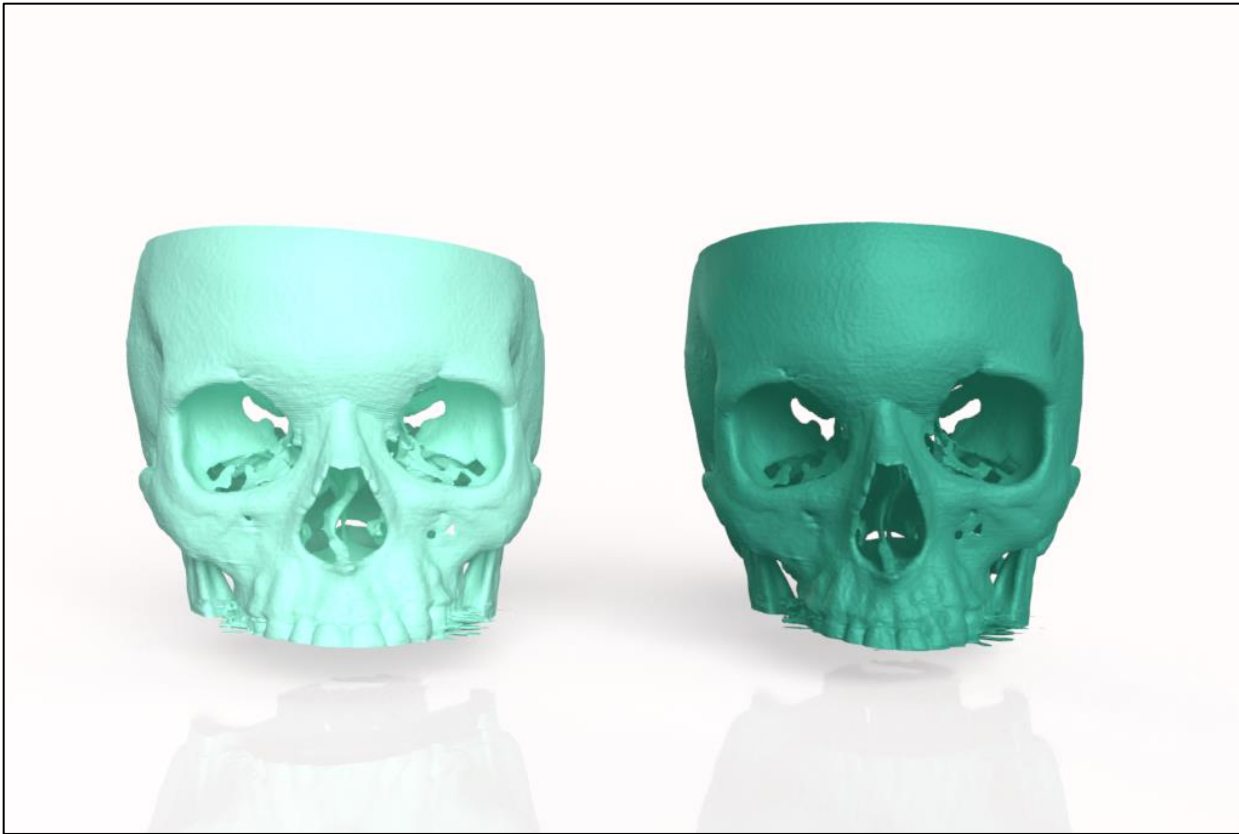


FIGURE 18: Surface meshes representing the shape consistent with the landmark configurations of the PC2 minimum (left) and maximum (right).

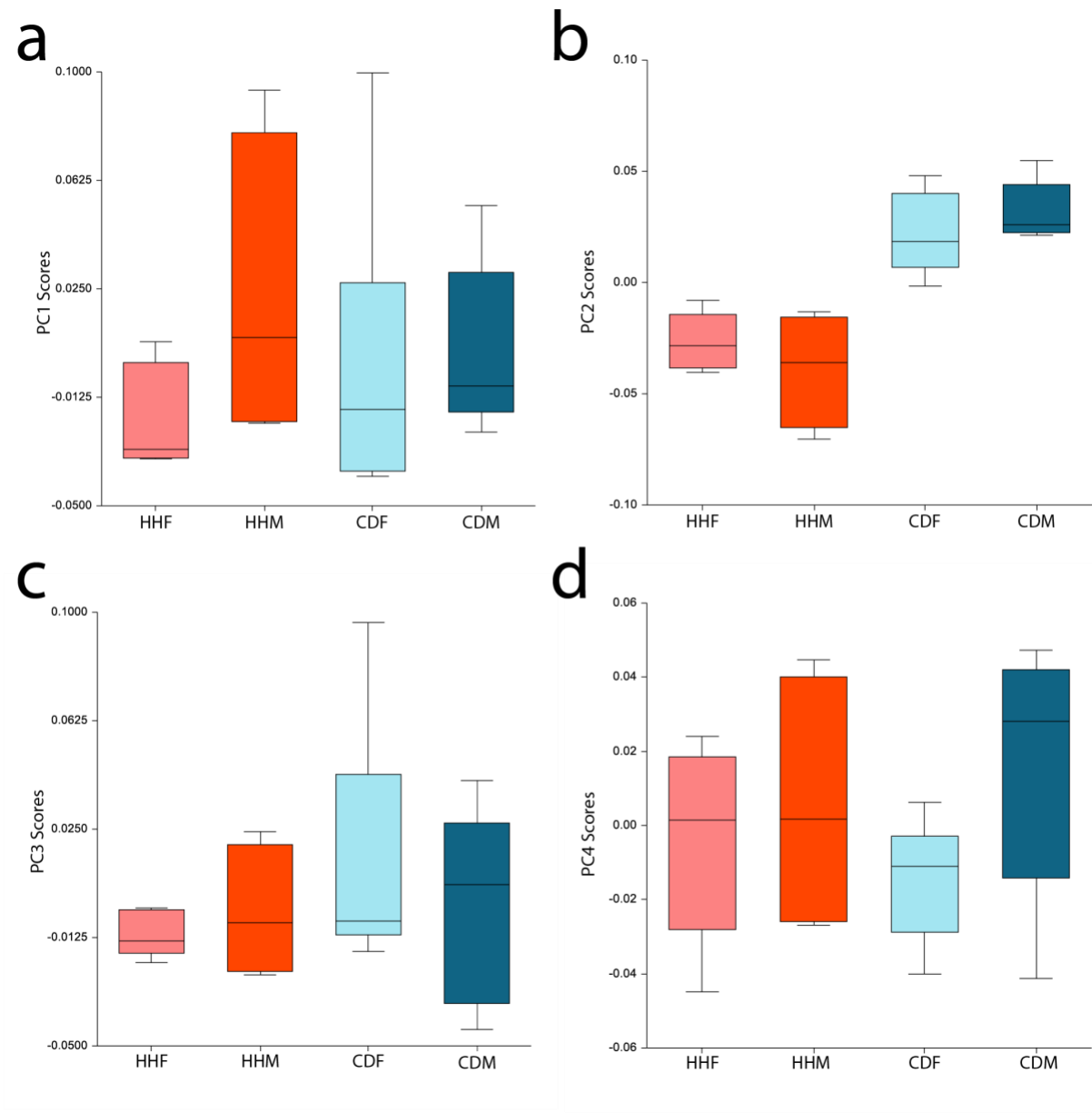


FIGURE 19: Box Plots of craniofacial surface PC1 scores by group (a), PC2 scores by group (b), PC3 scores by group (c), and PC4 scores by group (d).

Section 3: Facial Surface

On evaluation of the facial surface PC1 accounted for 38.21% of the variation, PC2 accounted for 17.57% of the variation, and PC3 accounted for 12.32% of variation. A plot of the

PC1 scores displays CD individuals clustered toward the PC1 minimum and HH individuals clustered towards the PC1 maximum with no overlap of descended groups. PC1 contrasts relative length (anteroposterior) and width dynamics. Subjects scoring at the PC1 minimum show a narrower external nose, particularly across the nares, and greater protrusion of the nose from the face. This is contrasted by those scoring at the PC1 maximum in which the external nose appears flatter and wider with wider set nares. The PC2 plot for the facial surfaces does not show any apparent clustering or groupings by descent or sex. The plot for PC3 shows a tendency for females to approach the maximum while males approach the minimum, though there is overlap between the two.

Results of the Kruskal-Wallis test for facial surface centroid sizes were nonsignificant ($\chi^2 = 5.25$ p=0.15). PC1 scores were significant ($\chi^2 = 16.28$ p=**0.001**) with the differences occurring between HHF and CDM (z=2.62, p < **0.05**), HHM and CDF (z=2.88, p < **0.05**), and HHM and CDM (z=3.60, p < **0.05**). PC2 ($\chi^2 = 4.59$ p=0.20) and PC3 ($\chi^2 = 3.97$ p=0.26) scores did not display significant differences between groups.

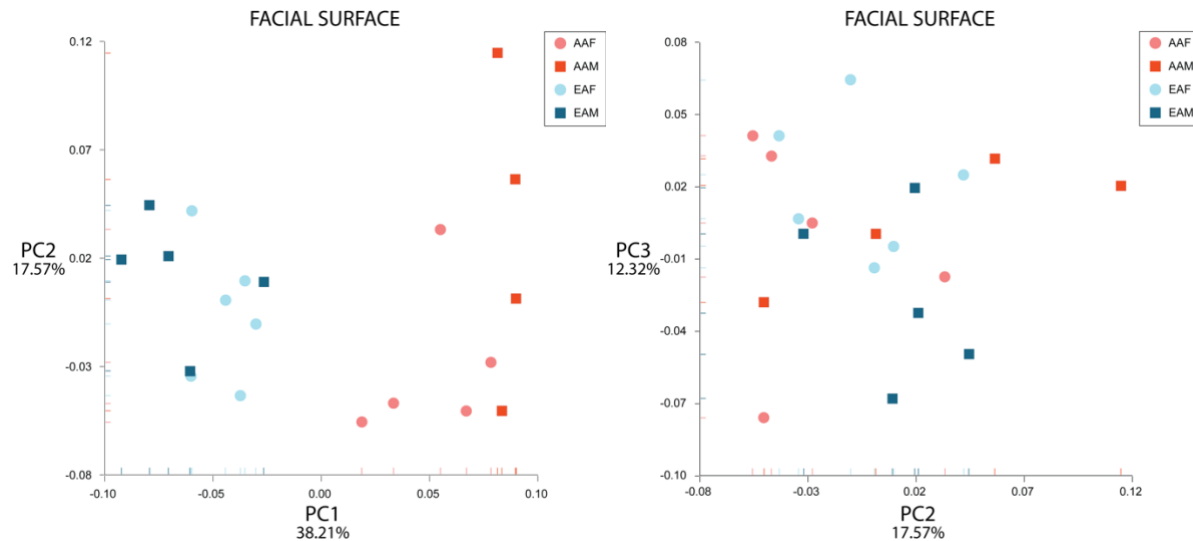


FIGURE 20: PCA plots for the facial surface where PC1 against PC2 is shown on the left and PC2 against PC3 is shown on the right.

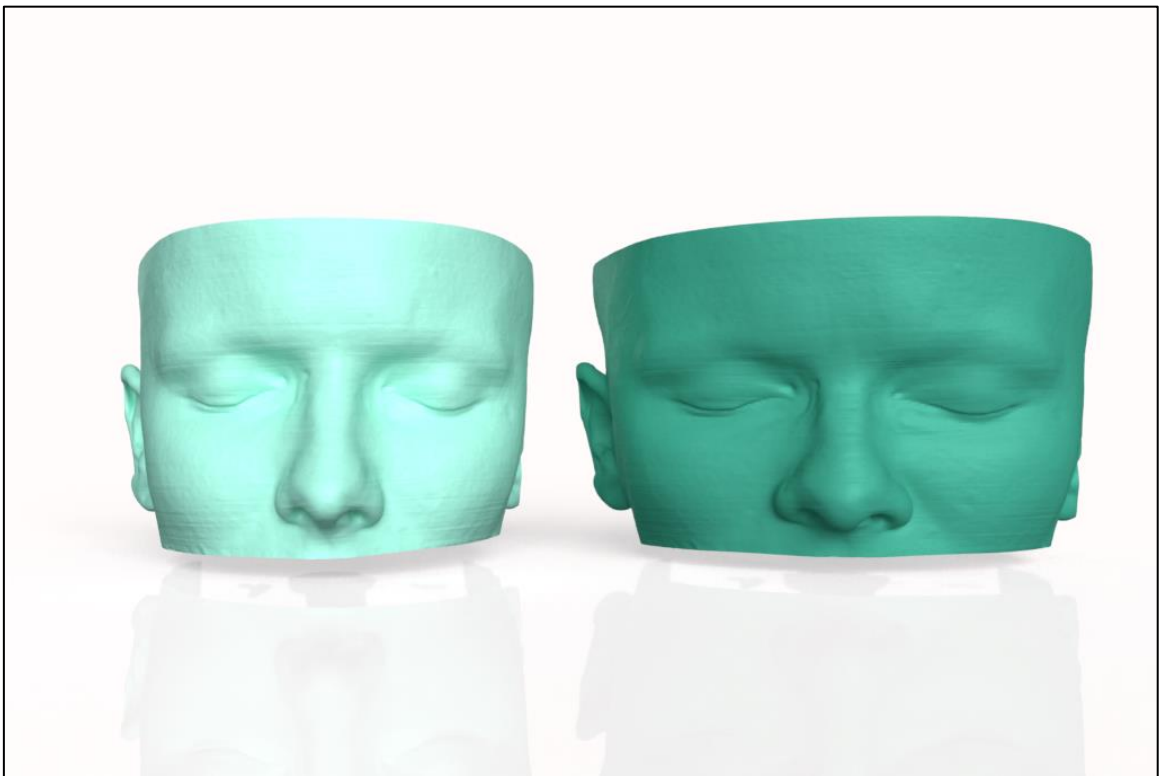


FIGURE 21: Surface meshes of the shapes consistent with the landmark configurations of the PC1 minimum (left) and maximum (right).

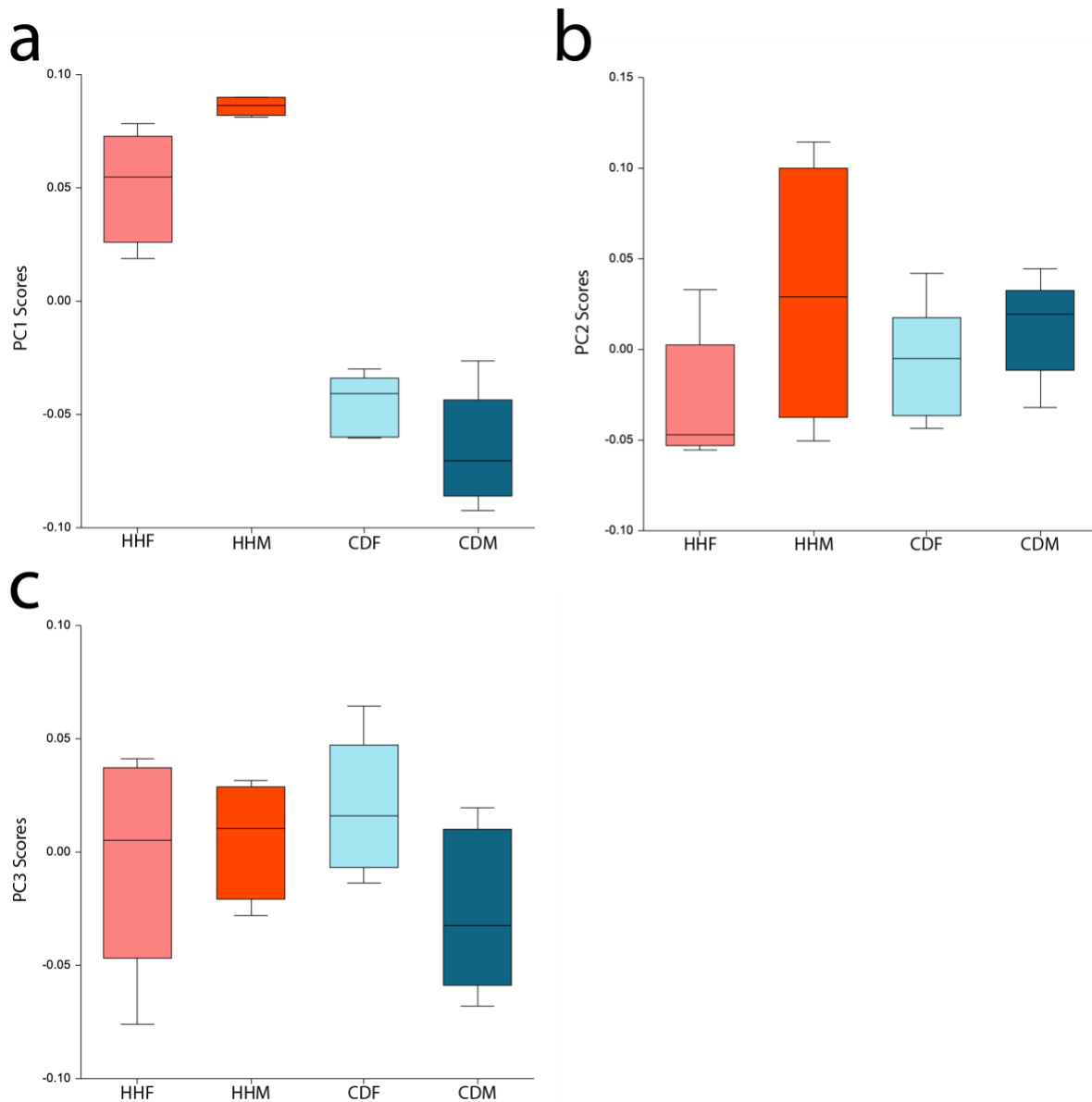


FIGURE 22: Box plots of the facial surface PC1 (a), PC2 (b), and PC3 (c) scores by group.

Section 4: Linear Measurements on the Craniofacial Surface

Tests for significant differences on linear measurements found no significant differences between any groups for external nasal height, internal nasal height, choanal height, inferior nasal fossa breadth, or choanal alare breadth. Distances of the nasal alare breadth reached significance

$\chi^2 = 11.80$, **p=0.008**) and found the differences occurred between HHF and CDF ($z=3.16$, **p < 0.05**) and HHM and CDF ($z=2.44$, **p < 0.05**).

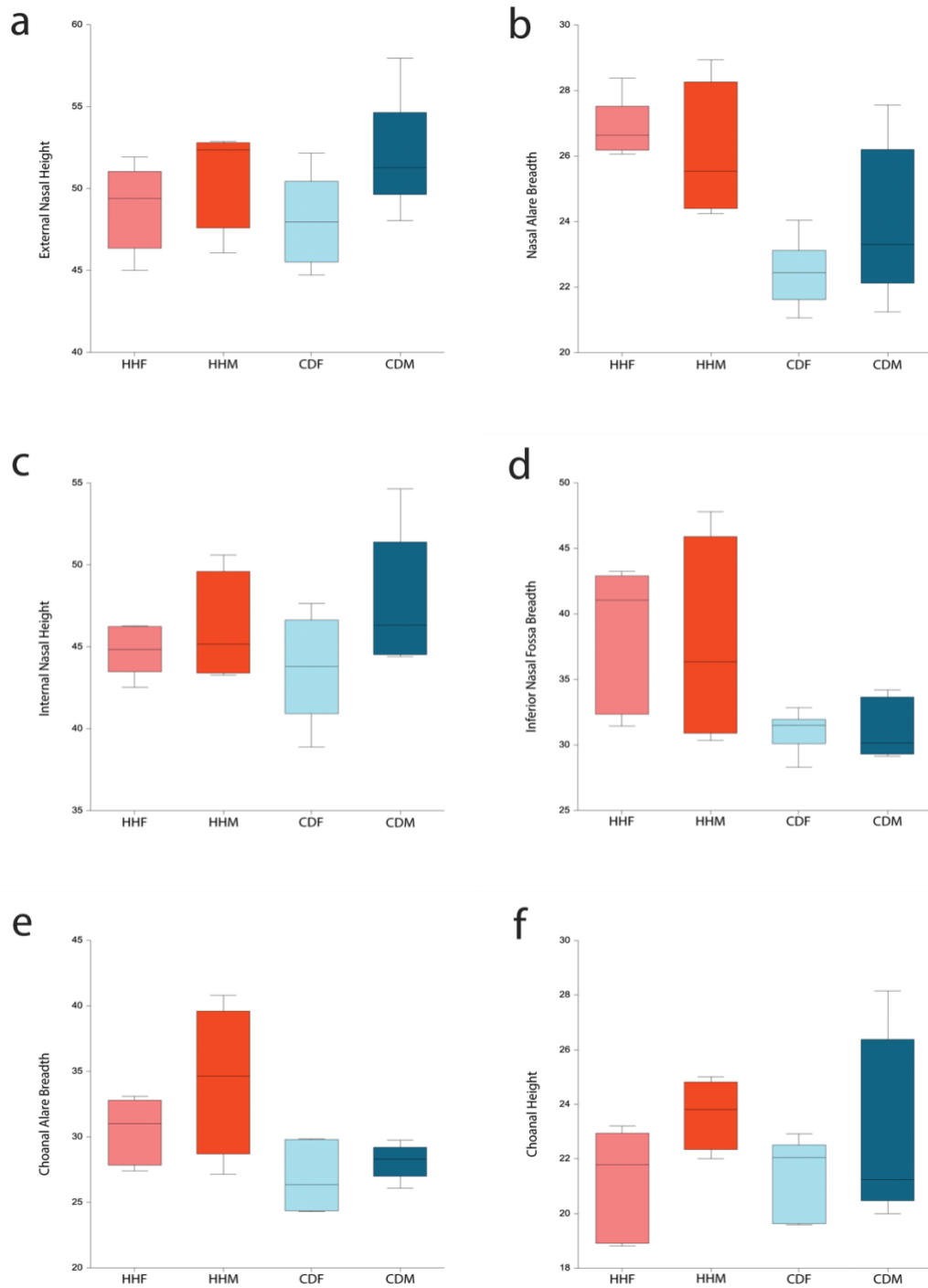


FIGURE 23: Box plots of the linear measurements by groups.

CHAPTER IV: DISCUSSION

The primary aim of this project was the development of a methodology to evaluate variation in shape of the decongested nasal passages using semi-landmark based 3D geometric morphometrics. A method capable of comprehensively assessing the morphology of the soft-tissue nasal passages was successfully developed. This involved obtaining 3D models of the decongested nasal passages, craniofacial bones, and external nasal structures, placing landmarks and semilandmarks to each of the models, collecting linear distance measurements, aligning all the landmark configurations via a general procrustes analysis, and analyzing shape variation with a principal component analysis. Finally, significant differences were evaluated between groups for principal component scores, centroid sizes, and linear distance measurements with the Kruskal-Wallis ANOVA and Dunn's Test. This method thus permits functionally relevant areas of the nasal airways to both be 1) accurately quantified, and 2) easily visualized. Once developed, this methodology was then employed to assess shape variation in the 3D decongested nasal passages between individuals of differing ecogeographic descent (e.g., cold-dry vs hot-humid) to determine whether the new developed method could detect the same patterns of nasal morphology as previously demonstrated by earlier studies (e.g Carey and Steegman, 1981; Franciscus and Long, 1991; Noback et al., 2011; Yokley, 2009; Marks et al., 2019). The overall results confirm that the new methodology is able to accurately detect the same patterns of ecogeographic variation in nasal morphology identified by previous studies, while providing more effective visualization of these morphological differences.

The PCA results of both the nasal passages surface (NPS) and craniofacial surface (CFS) analyses align with our first objective; confirming the method's ability to detect differences in overall height, breadth, and length dimension in the decongested nasal passages. Indeed, NPS PC1 results reveal that, compared to HH individuals, the CD individuals possess passages that are relatively long and narrow, while PC2 shows that CD individuals also possess passages that are relatively long and tall. Further, CFS PC2 (15.84%) scores show a clear separation between HH individuals clustered toward the minimum (relatively short and wide nasal apertures) and CD individuals clustered toward the maximum extreme (relatively tall and narrow apertures). Cumulatively, these results support previous assertions (Franciscus and Long, 1991; Noback et al., 2011; Yokley, 2009; Maddux et al., 2016) that individuals ancestrally derived from colder-drier environments (e.g., Europe) typically possess nasal passages that are relatively taller, narrower, and longer compared to individuals derived from tropical environments (e.g., West Africa) with shorter, wider and shallower nasal passages.

In relation to the second objective, the method's ability to detect morphological differences in the meatus morphology across decongested nasal passages was also confirmed, as indicated by our NPS PCA results. For NPS PC1, the common, inferior, and middle meatuses follow the general tendency for the nasal passages overall to be relatively narrow and long in CD individuals and wide and short in HH individuals. NPS PC2 results reveal a similar pattern, with CD individuals displaying relatively tall and narrow meatuses compared to the relatively short and broad meatuses seen in HH individuals. As meatus dimensions have rarely been examined in either anthropological or clinical research (but see Marks et al., 2019), these results provide tentative evidence that meatus dimensions generally conform to ecogeographic expectations for

overall nasal passage height/breadth/length dynamics (Yokley, 2009; Noback et al., 2011; Maddux et al., 2017, Marks et al., 2019).

For the final objective, the efficacy of the method in detecting ecogeographic variation in the external nasal anatomy was also shown by the PCA results of both the CFS and facial surface (FS). Specifically, the CFS PC2 shows that, in addition to possessing relatively tall and narrow nasal apertures, CD individuals generally exhibit nasal bones that protrude further from the surrounding craniofacial bones compared to individuals of HH descent. Additionally, for FS PC1, CD individuals cluster toward the minimum extreme (relatively narrower and more protruding), while HH individuals clustered toward the maximum extreme (relatively wider and flatter). These results appear to generally support the conclusions of Carey and Steegmann (1981), who demonstrated that populations indigenous to cold-dry environments predictably possess more projecting external noses compared to populations from warmer, more humid environments.

While this study was unable to identify evidence of sexual dimorphism in either CFS or FS centroid sizes, some evidence for significant differences in overall NPS size was found. Specifically, both HH and CD females exhibited significantly smaller NPS centroid sizes compared to CD males. HH males were also found to possess larger overall NPS centroid sizes compared to both CD and HH females (see Appendix E, Table E7), but this difference was not found to be statistically significant, possibly due to the particularly small number of individuals ($n = 4$) comprising the HH male sub-sample. In general, the results of the current study are concordant with those of a previous investigation by Bastir et al. (2020) into sexual dimorphism in the nasal passages. This previous study found significant differences between males and females in centroid sizes and in several functional regions of the nasal airway. These authors

suggested that differences in overall nasal passage size were likely attributable to metabolic differences related to oxygen intake requirements, with males requiring larger airways in order to inhale larger volumes of air with CD CH breadth (see also Hall, 2005; Holten et al., 2014). The current study thus potentially provides additional support for this assertion. However, additional studies investigating nasal morphology in direct association with metabolic data is necessary to more fully evaluate this hypothesis (Holten et al., 2014; Kelly et al., 2020).

This practicum continues the ongoing development of a methodology for assessing shape variation in the soft tissue nasal passages using 3D modeling. The methodology began with Elizabeth Thai's 2020 Internship Practicum, where she developed initial procedures for creating 3D models of decongested nasal passages (i.e., digitally controlling for variability in congestion of the soft tissues lining the nasal passages). These decongested models of the nasal passages were used in this practicum to further develop quantitative methods for assessing ecogeographic variation in the soft tissue lined nasal passages. Previous research into nasal morphology has predominantly focused on the bony boundaries of the nasal cavity within the craniofacial surface. These studies, while informative, have failed to provide information on the contributions of the soft tissues to the size and shape of the nasal passages (see Yokley, 2009 for a review). The advancement of medical imaging via CT scans has allowed more detailed and informative data relating to the complex 3D morphology of the nasal passages to be obtained, while technological advancements in 3D modeling and semilandmark-based geometric morphometrics provide new analytical approaches for morphological assessment. The use of semilandmarks in this practicum demonstrates the utility of semilandmark curves and surfaces for assessing morphological variability in both internal and external nasal morphology. This represents an important methodological contribution, as the complex 3D structure of the nasal passages is predominantly

comprised curved and non-planar surfaces that cannot be fully evaluated through linear measurements or even traditional (non-semilandmark) geometric morphometric methods.

The decongested nasal passage models assessed in this study will soon be employed in computational fluid dynamics (CFD) analyses of nasal airflow by the Dennis Lab at the University of Texas at Arlington. These CFD analyses will provide insights to how air flows through the nasal passages, as well as how humidity and temperature change during air passage through the nasal structures. When combined with the quantitative analyses of morphology provided by this practicum, these CFD results will provide the ability to precisely assess form-function relationships between nasal anatomy and airflow physiology for the first time. Accordingly, this research will help further inform future investigations into how variation in nasal morphology impacts the physiological function of the nasal tissues in warming and humidifying inspired air (and heat and moisture recapture during exhalation). It is thus anticipated that this research will meaningfully contribute to a greater understanding of how climatic variables have influenced nasal morphology across differing geographies and environments during human evolution in the near future.

CHAPTER V: SUMMARY AND CONCLUSION

This study used 3D modeling and semilandmark geometric morphometrics to evaluate shape variation in the nasal passages and the associated skeletal and external nasal structures. Due to limitations in technology and study designs, most previously conducted research of variation in the nasal passages has relied on linear distance measurements or morphometrics of the craniofacial surface. These limited methods could not account for the soft tissue of the nasal passages, and they are unable to capture accurate information regarding shape particularly in structures that have curved and nonplanar surfaces. This methodology was developed to use advances in CT imaging to develop 3D models for a more comprehensive analysis of shape variation. This methodology in combination with CFD analysis has the potential to provide a better understanding of the relationships between ecogeographic variations in nasal morphology, air flow dynamics, and nasal function as it pertains to conditioning air and recapturing heat and moisture.

Our results did identify qualitative and quantitative differences between our hot-humid, and our cold-dry representative groups. Differences were notable in the height, breadth, and length of the nasal passages, with the CD group displaying taller, narrower, and longer nasal passages and external nasal structures that had greater protrusion from the face compared to the HH group. These findings supported our three hypotheses: 1) CD nasal passages would be taller, narrower, and longer than HH, 2) CD common, inferior, and middle meatuses would be taller,

narrower, and longer than HH, and 3) CD would have narrower external nasal structures with greater protrusion from the face than HH.

Our results are consistent with previous observations of ecogeographic variation in the nasal passages. Additionally, our results indicate differences in the heights and breadths of the common and inferior meatuses, identifying locations to assess more in-depth in the future.

In conclusion, the methodology developed in this practicum resulted in a comprehensive evaluation of ecogeographic variation in nasal morphology, with qualitative and quantitative result indicating differences between our groups. Based on our results this methodology shows promise for future use with a larger sample size to satisfy the needs for more appropriate significance testing. This methodology will be utilized in the future as a component of ongoing research assessing ecogeographic variation in the soft tissue nasal passages and variation in airflow in the soft tissue nasal passages. This ongoing study will further advance our understanding of the relationship between nasal morphology and airflow dynamics in the nasal passages.

CHAPTER VI: INTERNSHIP EXPERIENCE

The internship practicum was part of the requirement for the degree of Master of Science in Medical Sciences at the University of North Texas Health Science Center in Fort Worth, Texas. The internship took place over the course of one year and was directly supervised by Scott Maddux, Ph.D. I started the internship after transferring to the Medical Sciences Research Track program in May 2020. Between May 2020 and July 2020, I worked with Dr. Maddux reviewing literature on the anatomy, physiology, evolution, and thermoregulatory functions of the nasal passages, as well as exploring a variety of computer software programs that would be useful for my future project. During this time I also prepared my applications for admission to medical schools as a dual degree MD/Ph.D or DO/Ph.D student.

During August 2020 I attended the AVIZO Short course present by the University of Texas High-Resolution X-ray Computed Tomography Facility. In September 2020, I completed a course in Head and Neck Anatomy with students at the Texas College of Osteopathic Medicine (TCOM). During November and December, I began my applications to Biomedical Sciences Ph.D. programs. In November 2020, I presented my proposal for my practicum research in a seminar in the Center for Anatomical Sciences.

Throughout my internship experience, I attended weekly meetings with Dr. Maddux to coordinate and work on the plan for my practicum research. By August I reached the decision to develop a methodology for analyzing shape variation in the nasal passages utilizing geometric morphometrics and semilandmarks. I was provided the 3D models of decongested nasal passages

for our sample by Elizabeth Thai, who developed the methodology for creating these models during her Research Track internship practicum the year before. Throughout September and October, I worked on creating the additional 3D models of the facial surface and craniofacial surface. I also spent this finding a procedure to align the three 3D models with the original CT data in order to create a consistent orientation for placing landmarks and taking measurements across the subjects. In November and December, I primarily worked on data collection according to the plans I settled on using and began to learn the basics of using R and R Studio.

From January to March, I worked on performing the analysis using R and R Studio with guidance from Dr. Maddux and the assistance of Dr. Mitchell. I also contributed to an additional research project investigating maxillary sinus morphology, co-authoring a journal article with DO/PhD student Sarah Kim, Dr. Lauren Butaric (Des Moines University), and Dr. Maddux (which has subsequently been accepted for publication in the Anatomical Record). In March, I completed my final analysis and began generating graphics to be used to communicate our results. The results obtained have been presented in this practicum report. Additionally, an abstract of this project was accepted for the 2021 UNTHSC Research Appreciation Day.

This experience has been incredibly fulfilling and enjoyable. Further it has shown me my enthusiasm for research and prepared me to take the next step toward a career in biomedical research and academia.

APPENDIX A

Abbreviations

TABLE 1: Abbreviations and explanations

Abbreviation	Explanation
CAB	Choanal Alare Breadth
CD	Cold-dry representative
CDF	Cold-dry Female
CDM	Cold-dry Male
CFD	Computational Fluid Dynamics
CFS	Craniofacial Surface
CH	Choanal Height
CS	Centroid Size
CT	Computed Tomography
ENH	External Nasal Height
FS	Facial Surface
GPA	General Procrustes Analysis
HH	Hot-humid representative
HHF	Hot-humid Female
HHM	Hot-humid Male
INFB	Inferior Nasal Fossa Breadth
INH	Internal Nasal Height
NAB	Nasal Alare Breadth
NPS	Nasal Passage Surface
PC	Principal Component
PCA	Principal Component Analysis
PLY	Polygon File Format
STL	Standard Tessellation Language

APPENDIX B
METHODOLOGY GRAPHICS

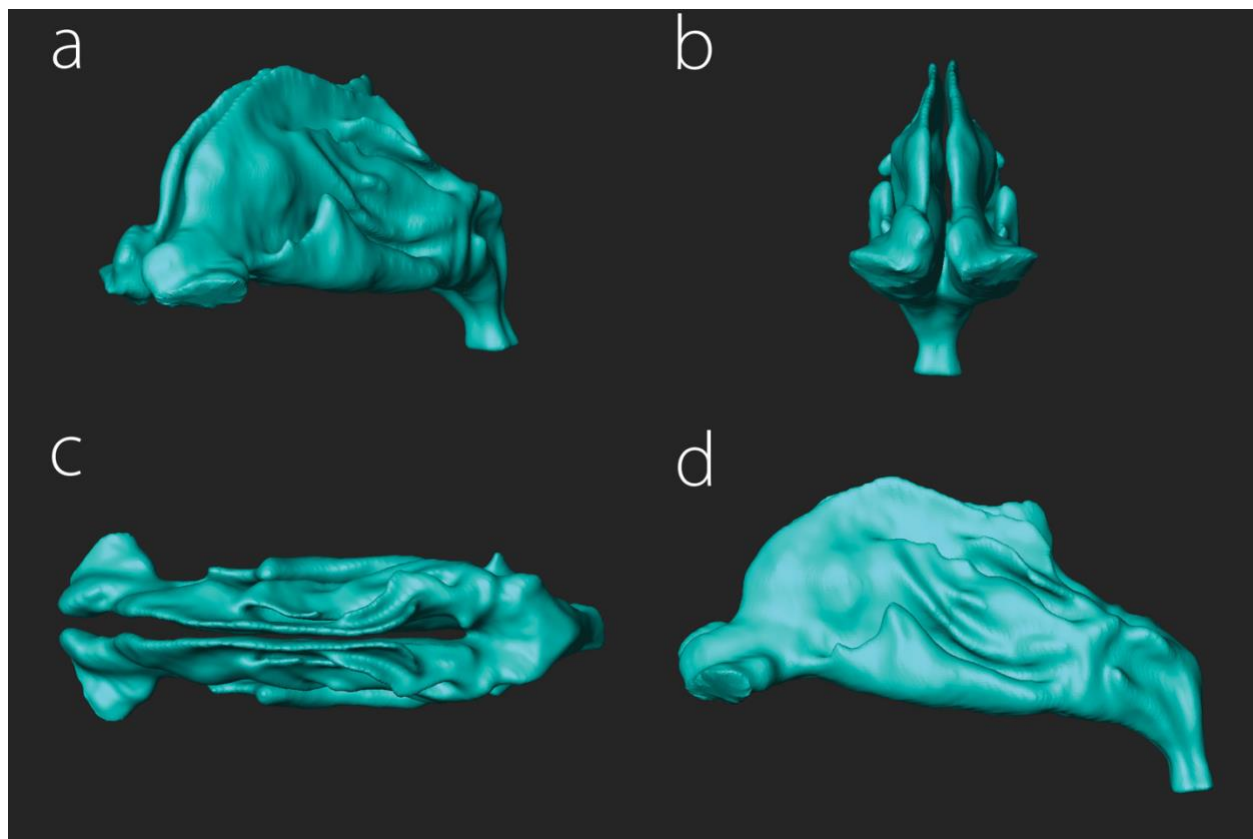


FIGURE B1: Example of a completed 3D model of the decongested nasal passages. a) anterolateral view, b) anterior view, c) superior view, d) lateral view.

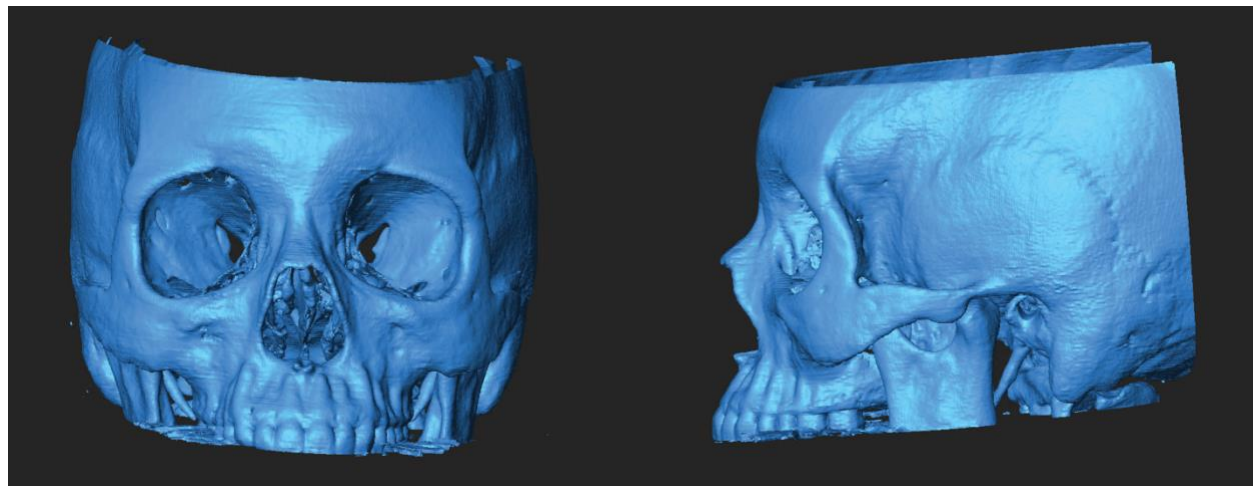


FIGURE B2: Example of the 3D model of the craniomaxillofacial surface from a frontal (left) and lateral view (right)

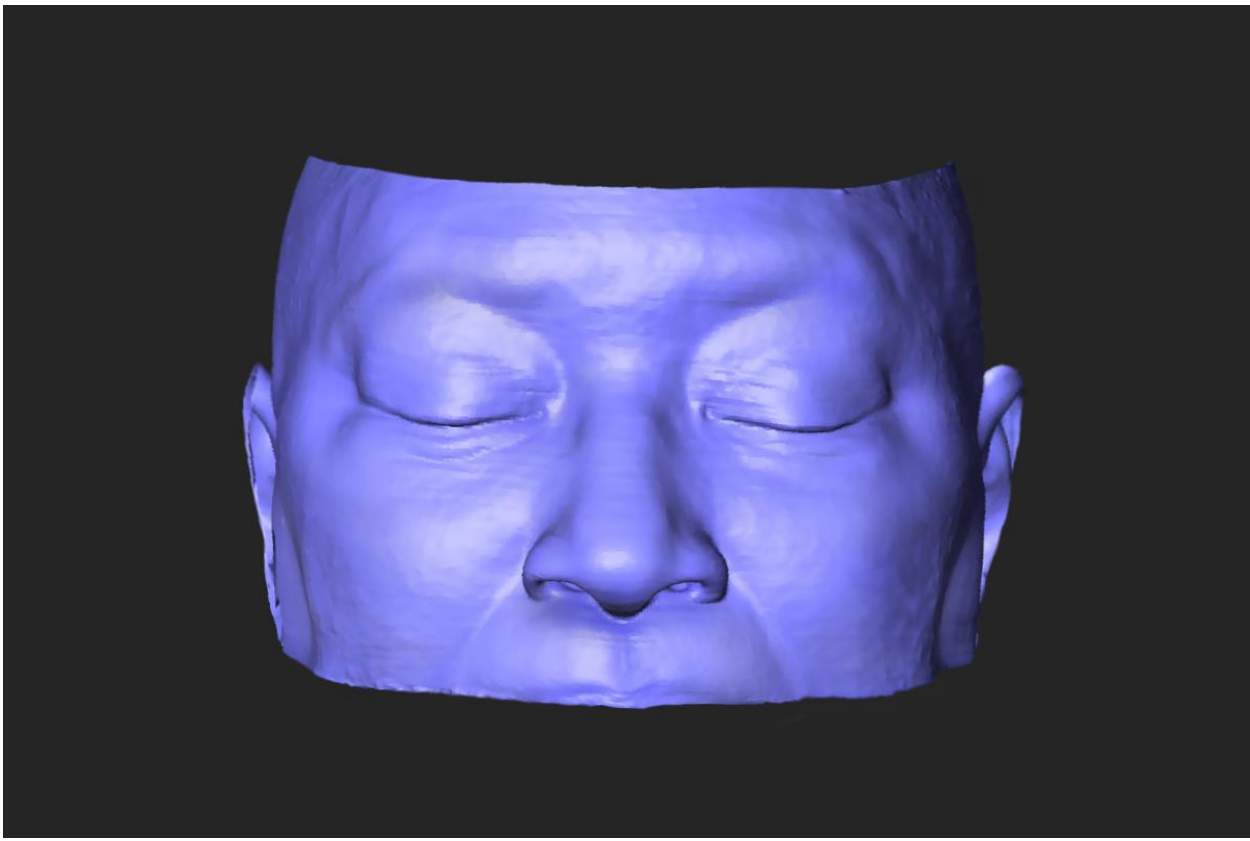


FIGURE B3: Example of a 3D model of the facial surface. This model has been modified as an example to maintain subject confidentiality, thus it is not a direct render of any individual in this study.

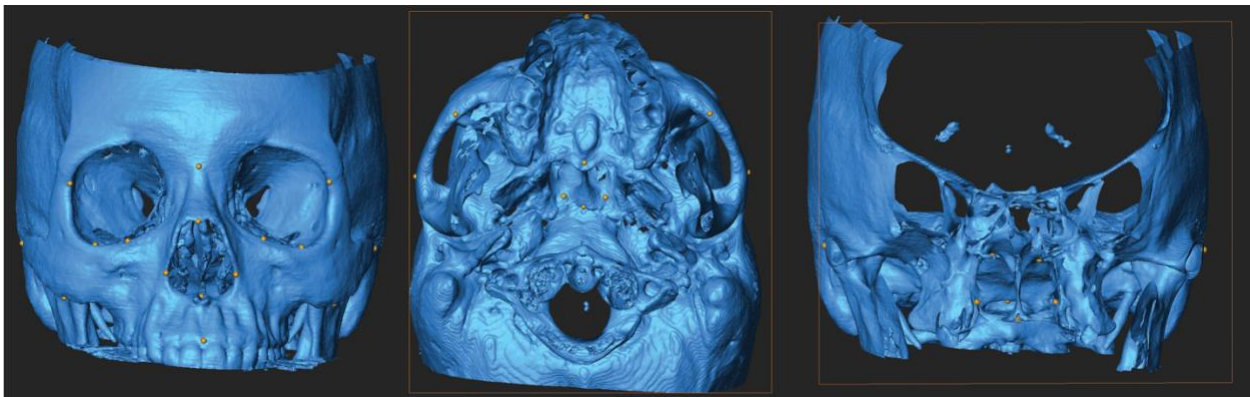


FIGURE B4: Example of the landmarks placed on the craniofacial bones and bony nasal cavity. Left) anterior view of the craniofacial landmarks, Middle) inferior view of the cranial landmarks, Right) an anterior view of the craniofacial surface with an overlying clipping place to visualize the choana and posterior landmarks.

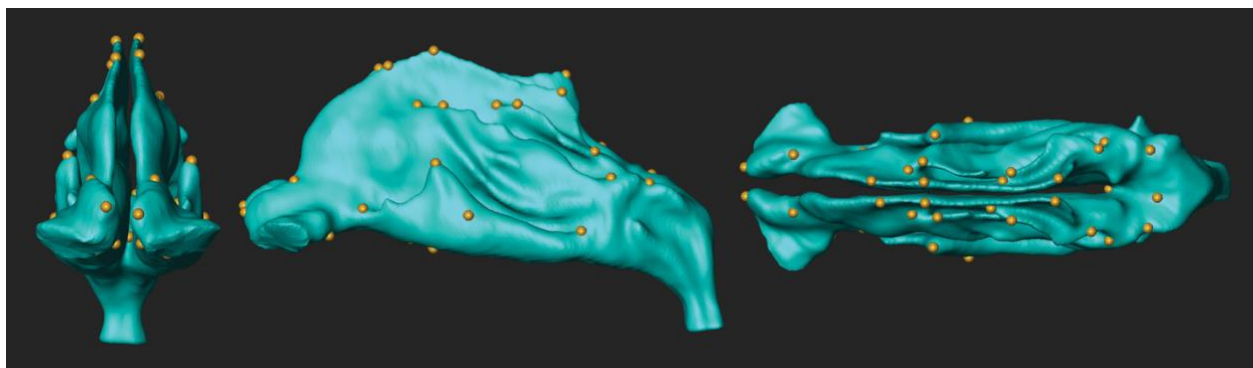


FIGURE B5: Anterior (left), lateral (middle), and superior (right) view of the Type II landmarks placed on the 3D model of the nasal passages

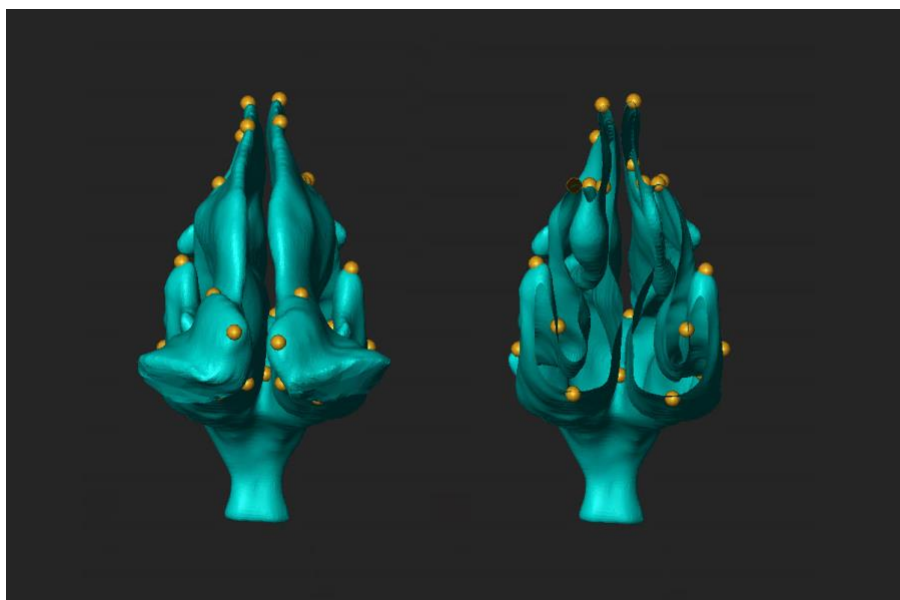


FIGURE B6: Anterior view of the nasal passage with type II landmarks (left), anterior view with an overlying clipping plane to view the landmarks on the medial aspect of the inferior meatus space and landmark at the posterior termination of the nasal septum (right).

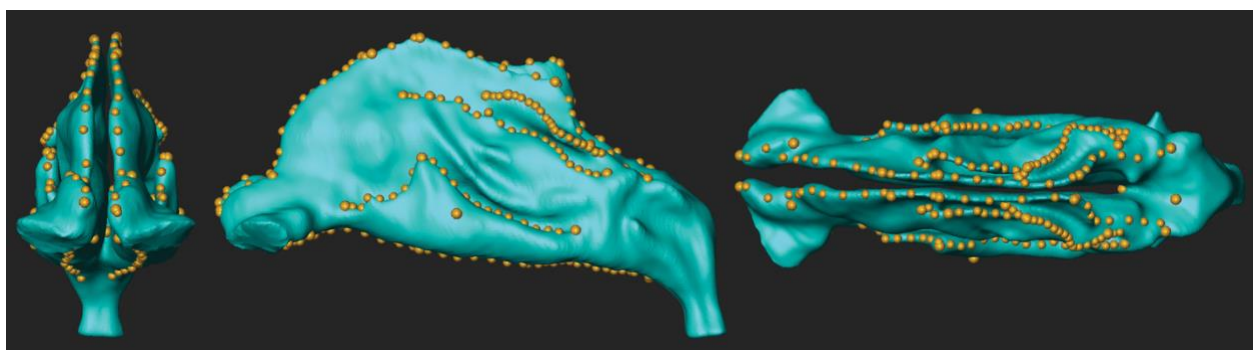


FIGURE B7: Anterior (left), lateral (middle), and superior (right) view of the type II landmarks and type III semilandmarks placed on the 3D model of the nasal passages

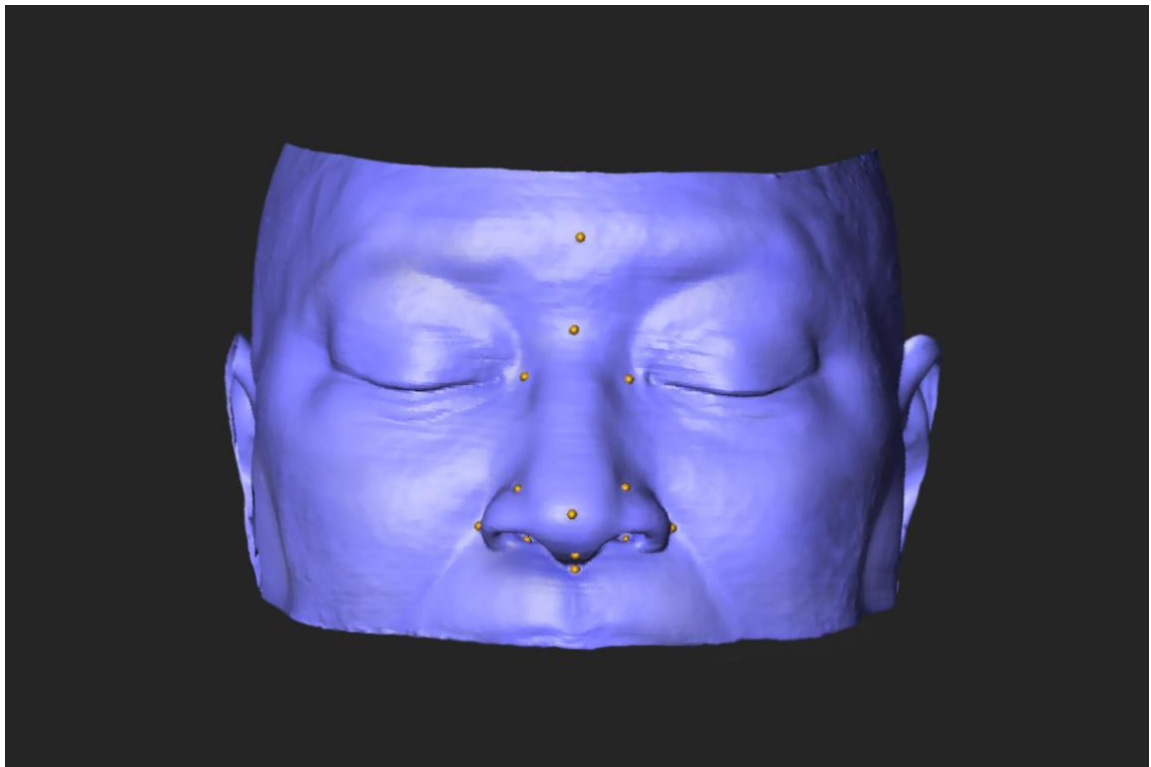


FIGURE B8: Example of the landmarks placed on the facial surface. Again, the underlying model has been altered to maintain subject confidentiality and does not represent an individual in the study.

APPENDIX C
LANDMARK DESCRIPTIONS

TABLE C1: Landmarks for the 3D model of the nasal passages

1, 2 (R, L)	Most anterior point of the Nasal vestibulum.
3, 18 (L, R)	Anterior most and superior most point of intersection of the inferior and common meatus
4, 19 (L, R)	Most superior point on the Lateral aspect of the Inferior Meatus.
5, 20 (L, R)	Posterior most and superior most intersection of the inferior and common meatus
6, 21 (L, R)	Anterior most and superior most point of intersection of the middle and common meatus
7, 22 (L, R)	Most superior point on the Lateral aspect of the middle meatus.
8, 23 (L, R)	Posterior most and superior most intersection of the middle and common meatus
9, 24 (L, R)	Anterior most and superior most point of intersection of the superior and common meatus
10, 25 (L, R)	Most superior point on the Lateral aspect of the superior meatus.
11, 26 (L, R)	Posterior most and superior most intersection of the superior and common meatus
12, 27 (L, R)	Superior most point of the nasal cavity, representative of the ethmoidal.
13, 28 (L, R)	Posterior most and Superior most point on the upper ridge of the nasal cavity.
14, 29 (L, R)	Point representing the Nasion, marked at the angular change along the superior curvature of the nasal cavity anterior to the superior most point of the nasal cavity.
15, 30 (L, R)	Inferior most point of the superior aspect of the nasal valve, in line with the superior curvature of the nasal vestibulum and nasal cavity.
16, 31 (L, R)	Superior most point within the choanal apex impression
17, 32 (L, R)	Superior most point on the inferior aspect of the nasal valve
33, 34 (R, L)	Medial and Inferior most point on the nasalcavity floor posterior to the nasal valve
35, 36 (R, L)	Medial and Inferior most point on the medial projection of the inferior meatus
37, 38 (L, R)	Inferior most point of the nasal cavity floor, directly below the most superior point
39, 40 (R, L)	Points associated with the widest breadth across the inferior nasal fossa.
41	Point just anterior to the termination of the nasal septum, or where the two cavities merge.
42	Posterior most point of termination of the choanal arches, approximating the hormion.

TABLE C2: Landmarks for the Craniofacial Surface.

1	Nasion	Most anterior portion of the suture between the frontal bone and the nasal bones.
2	Rhinion	Most anterior point of the suture line between the two nasal bones
6	Nasospinale	Point of intersection of the sagittal midline and the line representing the lowest point of the nasal opening.
5	Prosthion	Most anterior point of the sagittal midline of the alveolar process of the maxilla
3, 4 (R, L)	Nasal Alare	Points marking the widest breadth of the nasal aperture
7, 8 (R, L)	Zygoorbitale	Point of intersection of the zygomatic-maxillary suture with the inferior orbital rim.
9, 10 (R, L)	Orbitale	Lowest point on the inferior orbital rim.
11, 12 (R, L)	Frontomolare-orbitale	Medial most point of the suture between the frontal and zygomatic bones on the orbital rim.
13, 14 (R, L)	Zygion	Most lateral point on the zygomatic arch
15, 16 (R, L)	Zygomatico-maxillaire	Inferior point on the left suture of the zygomatic and maxillary bones
17	Basion	The anterior most point at the foramen magnum
18	Hormion	Point of Intersection between the sutures
19	Staphylion	Midpoint of the most anterior portion of the floor of the choanal opening.
20, 21 (R, L)	Choanal Apex	The most superior point of the choanal opening
22, 23 (R, L)	Choanal Alare	Point of widest breadth on the inferior ½ of the left choanal opening
24	Ethmoidal	Highest point of the internal nasal cavity.
25	Nasal Floor	Lowest point of the nasal floor directly below the ethmoidal.
26	Left Inferior Nasal Fossa Point	Point of widest breadth of the left nasal wall beneath the inferior turbinate
27	Right Inferior Nasal Fossa Point	Point of widest breadth of the right nasal wall beneath the inferior turbinate.

TABLE C3: Landmarks for the 3D model of the facial surface.

Glabella	Anterior most point along the midline of the sagittal plane between the superciliary arches.	Bastir et al. 2019
Nasion	Most anterior portion overlying of the suture between the frontal and the nasal bones on the skin.	Bastir et al. 2019
Nasal tip	Point of the highest curvature or prominence along the midsagittal line of the external nose.	Bastir et al. 2019
Columnella	Anterior most point on the midsagittal line of the columnella.	Bastir et al. 2019
Nasolabial junction	Point of transition between the inferior boundary of the columnella and the superior labial region.	Bastir et al. 2019
Supra-alar crease (R, L)	Superior most and Lateral most point on the ridge of the nasal wing.	Bastir et al. 2019
Lateral Ala (R, L)	The most lateral point on the ala nasi.	
Nostril base (R, L)	Proximal most point within the nares.	Bastir et al. 2019
Nasolacrimal curve (R, L)	Point of intersection of the nasofacial sulcus and a straight line between the left and right medial canthus.	

APPENDIX D

R scripts

Packages

```
> library(geomorph)
> library(Morpho)
```

Loading Data

```
> nps.data <- read.morphologika("NPS-morphologika-file.txt")
> semi.matrix <- read.csv("NPS-semilandmark-matrix.csv", header = T, sep = ",")
> links <- read.csv("NPS-links.csv", header = T, sep = ",")
> estimate.missing(nps.data)
```

Setting up factors

```
> descent <- as.factor(nps.data$labels[,1])
> sex <- as.factor(nps.data$labels[,2])
```

General Procrustes Analysis and Visualizations

```
> nps.gpa <- gpagen(nps.data$coords, curves = semi.matrix)
> summary(nps.gpa)
> plotOutliers(nps.gpa$coords)
> plotAllSpecimens(nps.gpa$coords, mean = T, links = links, label = T, plot.param = list(pt.bg = "#4bc649", pt.cex
= 0.2, mean.bg = "#004901", mean.cex = 0.8, link.col="#004901", link.lwd= 0.5, link.lty = 1,
txt.pos = 2, txt.cex = 1, txt.col = "#000000"))
>
> nps.Csize <- nps.gpa$Csize
> print(nps.Csize)
>
> nps.mn <- mshape(nps.gpa$coords)
> plotRefToTarget(nps.mn, nps.gpa$coords[,X], gridPars = shape.pp, method = "vector", label = T)
```

Principal Component Analysis

```
> nps.pca <- gm.prcomp(nps.gpa$coords)
> summary(nps.pca)
> plot(nps.pca, main ="PCA", pch = c(19,15)[sex], col = c("#f55352", "#106188")[descent], cex=1.2)

> legend(-0.15, 0.2, legend = c("AAF", "AAM", "EAF", "EAM"), col=c("#f55352", "#f55352", "#106188",
"#106188"), pch= c(19, 15, 19, 15), cex=1.2, bty="n", yjust = 5)

> plotRefToTarget(nps.pca$shapes$shapes.comp1$min, nps.pca$shapes$shapes.comp1$max, gridPars= pca.pp,
method="points", links = links, axes = T)
>
> nps.PCscores <- as.matrix(nps.pca$x)
> print(nps.PCscores)
```

Establishing surface mesh of mean shape

```
> findMeanSpec(nps.gpa$coords)
> mean.sub.lmks <- as.matrix(read.csv("NPS-MeanSub-lmks.csv", header = T, sep = ",", strip.white = T))
```

```
> mean.sub.ply <- read.ply("MeanSub-NPS-ascii.ply")
> mean.mesh <- warpRefMesh(mean.sub.ply, mean.sub.lmks, nps.mn, color = "#7f92cc", centered = FALSE)
```

Obtaining PC extreme surface meshes

```
> nps.PC1max.ply <- plotRefToTarget(nps.mn, nps.pca$shapes$shapes.comp1$max, mesh=mean.mesh,
   method= "surface", alpha = 0.5)
>
> mesh2ply(nps.PC1min.ply)
```

Plotting Parameters

```
> pca.pp <- gridPar(pt.bg = "#f55352", pt.size = 0.7, link.col="#f55352", link.lwd= 0.7, link.lty = 1, tar.pt.bg =
  "#5edee5", tar.pt.size = 0.7, tar.link.col="#5edee5", tar.link.lwd= 0.7, tar.link.lty = 3, txt.pos = 2,
  txt.cex = 1, txt.col = "#000000")

> shape.pp <- gridPar(pt.bg = "#4bc649", pt.size = 0.7, link.col="#4bc649", link.lwd= 0.7, link.lty = 1, tar.pt.bg =
  "#004901", tar.pt.size = 0.7, tar.link.col="#004901", tar.link.lwd= 0.7, tar.link.lty = 2, txt.pos = 3,
  txt.cex = 1, txt.col = "#000000")
```

[Data Objects](#), [GPA Data Object](#), [PCA Data Object](#), [Mean Shape Object](#)

[Commands](#)

[File names](#)

[Attributes](#)

APPENDIX E
RESULTS

TABLE E1: Principal component analysis proportion of variance results for all three surfaces

Principal Component	Proportion of Variance	Cumulative Proportion
Nasal Passage PC1	19.13%	0.1913
Nasal Passage PC2	14.20%	0.3331
Nasal Passage PC3	10.68%	0.4400
Craniofacial Surface PC1	21.93%	0.2193
Craniofacial Surface PC2	15.84%	0.3777
Craniofacial Surface PC3	12.26%	0.1226
Craniofacial Surface PC4	10.92%	0.5003
Facial Surface PC1	38.21%	0.3821
Facial Surface PC2	17.57%	0.5577
Facial Surface PC3	12.32%	0.6809

Only principal components accounting for greater than 10% of the variance were reported.

TABLE E2: Principal component scores for the nasal passages for all individuals

ID	Descent x Sex	NPS PC1	NPS PC2	NPS PC3
Y002	CDM	-0.001177515	0.03901862	0.01102372
Y003	CDF	-0.015039624	0.009583527	-0.0400027
Y004	HHF	-0.075936242	-0.016144738	0.02541853
Y005	CDF	0.001141828	0.090478335	0.02767992
Y012	HHF	-0.056513317	-0.013447404	-0.06742031
Y013	HHM	-0.04817918	0.045562046	0.01179683
Y015	HHM	0.015700808	-0.034261534	0.08440041
Y023	CDM	0.02956307	0.073616408	-0.0170452
Y045	CDF	-0.00606573	0.026204472	-0.03969855
Y055	CDM	0.105061925	0.003464002	-0.01204576
Y056	HHF	-0.002594653	-0.024256653	-0.04614032
Y071	CDF	0.013400128	0.029585077	0.01808049
Y083	CDM	0.043488044	0.036866122	0.03283212
Y087	CDM	0.136633816	-0.100942244	-0.0536956
Y093	CDF	-0.002996348	0.078597719	-0.01793296
Y101	CDF	0.036076795	-0.029167381	-0.01239196
Y105	HHF	-0.057259876	-0.055991673	-0.05642919
Y109	HHF	-0.093115592	-0.036054868	-0.00384997
NM304	HHM	0.069247156	-0.039291733	0.09231332
NM30	HHM	-0.091435492	-0.0834181	0.0631072

TABLE E3: Significance testing for the nasal passage principal component scores

		PC1	PC2	PC3
Hot-Humid Female	Mean	-0.057084	-0.029179	-0.029684
	Median	-0.057260	-0.024257	-0.046140
	Z- Value	-2.58		-1.70
Hot-Humid Male	Mean	-0.013667	-0.027852	0.062904
	Median	-0.016239	-0.036777	0.073754
	Z- Value	-0.19		2.65
Cold-Dry Female	Mean	0.004420	0.034214	-0.010711
	Median	-0.000927	0.027895	-0.015162
	Z- Value	0.17		-0.50
Cold-Dry Male	Mean	0.062714	0.010405	-0.007786
	Median	0.043488	0.036866	-0.012046
	Z- Value	2.58		-0.22
p- value		0.019	0.129	0.046

Bold Z-values are significant by Dunn's Test ($z > 1.960$), Italicized are also significant by Bonferroni Test ($z > 2.6383$)

TABLE E4: Principal component scores for the craniofacial surface for all individuals

	Descent x Sex	PC1	PC2	PC3	PC4
Y002	CDM	-0.010646105	0.026012796	0.005869794	0.047239371
Y003	CDF	-0.037313734	0.047998986	-0.005507377	-0.005793904
Y004	HHF	0.006575974	-0.036446945	-0.013555209	0.001503372
Y005	CDF	-0.024819214	0.011357027	0.02639829	-0.040102563
Y012	HHF	-0.033830606	-0.02072722	-0.014718929	0.023990034
Y013	HHM	-0.021612499	-0.013009045	-0.020090117	0.026732158
Y015	HHM	0.093569654	-0.049076793	0.005465225	0.044621416
Y023	CDM	-0.008717021	0.033527305	0.012035381	0.013052651
Y045	CDF	0.002984955	0.009323017	0.096368575	-0.012943917
Y055	CDM	0.053657317	0.05460686	-0.026201232	-0.041356246
Y056	HHF	-0.007343931	-0.007851423	-0.002197207	0.012920212
Y071	CDF	0.099803704	0.025644561	-0.009810536	-0.024989746
Y083	CDM	0.007966004	0.023716923	0.041934747	0.036718363
Y087	CDM	-0.024469189	0.021368057	-0.044310202	0.028014549
Y093	CDF	-0.039841749	0.03749049	-0.008299759	-0.009350681
Y101	CDF	-0.008353933	-0.001554872	-0.017417128	0.006296565
Y105	HHF	-0.030495305	-0.040514643	-0.003488103	-0.011367415
Y109	HHF	-0.033268478	-0.028450252	-0.021283945	-0.044909059
NM304	HJM	0.035399386	-0.022850319	-0.025399461	-0.023408018
NM030	HJM	-0.01924523	-0.070564508	0.024207192	-0.026867141

TABLE E5: Significance testing for the craniofacial surface principal component scores

		CFS PC1	CFS PC2	CFS PC3
Hot-Humid Female	Mean	-0.019672	-0.026798	-0.019672
	Median	-0.030495	-0.028450	-0.030495
	Z- Value		-2.14	
Hot-Humid Male	Mean	0.022028	-0.038875	0.022028
	Median	0.008077	-0.035964	0.008077
	Z- Value		-2.36	
Cold-Dry Female	Mean	-0.001257	0.021710	-0.001257
	Median	-0.016587	0.018501	-0.016587
	Z- Value		1.82	
Cold-Dry Male	Mean	0.003558	0.031846	0.003558
	Median	-0.008717	0.026013	-0.008717
	Z- Value		2.40	
p- value		0.461	0.002	0.788

Bold Z-values are significant by Dunn's Test ($z > 1.960$), Italicized are also significant by Bonferroni Test ($z > 2.6383$)

TABLE E6: Principal component scores for the facial surface for all individuals

ID	Descent x Sex	PC1	PC2	PC3
Y002	CDM	-0.02653233	0.009060569	-0.06798935
Y003	CDF	-0.03738517	-0.04341171	0.041261139
Y004	HHF	0.01871049	-0.05554992	0.041253828
Y005	CDF	-0.05978544	0.041868573	0.024994621
Y012	HHF	0.05497819	0.033224171	-0.017373255
Y013	HHM	0.08956392	0.056435206	0.031752498
Y015	HHM	0.08990166	0.001373169	0.000491086
Y023	CDM	-0.06058694	-0.032125201	0.000519936
Y045	CDF	-0.03526454	0.00956511	-0.004742869
Y055	CDM	-0.07056791	0.020962502	-0.032370999
Y056	HHF	0.07830988	-0.028051821	0.005003177
Y071	CDF	-0.0301888	-0.010375707	0.064541942
Y083	CDM	-0.09233969	0.01937696	0.019573348
Y087	CDM	-0.07939812	0.044481741	-0.049467639
Y093	CDF	-0.06020543	-0.034402891	0.006756627
Y101	CDF	-0.04419175	0.000647355	-0.013630068
Y105	HHF	0.03332789	-0.046888215	0.032815893
Y109	HHF	0.06691376	-0.050484676	-0.075906814
NM304	HHM	0.08135474	0.114732348	0.020458703
NM030	HHM	0.08338559	-0.050437563	-0.027941804

TABLE E7: Results of significance testing for the facial surface principal component scores

		PC1	PC2	PC3
Hot-Humid Female	Mean	0.050448	-0.029550	-0.002841
	Median	0.054978	-0.046888	0.005003
	Z- Value	1.53		
Hot-Humid Male	Mean	0.086051	0.030526	0.006190
	Median	0.086475	0.028904	0.010475
	Z- Value	3.02		
Cold-Dry Female	Mean	-0.044504	-0.006018	0.019864
	Median	-0.040788	-0.004864	0.015876
	Z- Value	-1.49		
Cold-Dry Male	Mean	-0.065885	0.012351	-0.025947
	Median	-0.070568	0.019377	-0.032371
	Z- Value	-2.75		
p- value		0.001	0.204	0.264

Bold Z-values are significant by Dunn's Test ($z > 1.960$), Italicized are also significant by Bonferroni Test ($z > 2.6383$)

TABLE E8: Centroid sizes for all subjects

ID	Descent and Sex	Nasal Passage	Craniofacial Surface	Facial Surface
Y002	CDM	476.5193	239.1702	100.66158
Y003	CDF	409.9612	212.0245	84.99572
Y004	HHF	408.4239	225.7899	94.86821
Y005	CDF	435.2376	212.8964	89.50131
Y012	HHF	403.8157	212.1272	81.56343
Y013	HHM	426.63	223.5097	94.8814
Y015	HHM	421.9525	209.5614	89.17141
Y023	CDM	416.5987	217.3111	90.01992
Y045	CDF	401.9256	209.3482	83.09141
Y055	CDM	442.6135	218.5978	92.89189
Y056	HHF	431.9506	226.7585	100.28314
Y071	CDF	395.4941	219.6174	92.95532
Y083	CDM	445.1454	226.751	95.99433
Y087	CDM	460.4618	215.5989	87.03658
Y093	CDF	407.395	212.2772	85.45987
Y101	CDF	410.8553	207.3542	84.81183
Y105	HHF	419.0576	219.238	94.34478
Y109	HHF	413.7591	218.4845	85.76775
NM304	HHM	413.2821	220.5902	90.77669
NM030	HHM	436.1893	229.8956	93.46641

TABLE E9: Results of statistical significance tests for centroid sizes

		Nasal Passages	Craniofacial Surface	Facial Surface
Hot-Humid Female	Mean	415.4014	220.4796	91.36546
	Median	413.7591	219.238	94.34478
	Z- Value	-0.9165	0	0
Hot-Humid Male	Mean	424.5135	220.8892	92.07397
	Median	424.2913	222.05	92.12155
	Z- Value	0.6614	0	0
Cold-Dry Female	Mean	410.1448	212.253	86.80257
	Median	408.6781	212.1508	85.2278
	Z- Value	-2.3094	0	0
Cold-Dry Male	Mean	448.2677	223.4858	93.32086
	Median	445.1454	218.5978	92.89189
	Z- Value	2.7495	0	0
p- value		0.01557	0.10363	0.15466

Bold Z-values are significant by Dunn's Test ($z > 1.960$), Italicized are also significant by Bonferroni Test ($z > 2.6383$)

TABLE E10: Linear Measurements for all subjects

Subject ID	Descent x Sex	Nasion to Prosthion	External Nasal Height	Nasal Alare Breadth	Internal Nasal Height	Inferior Nasal Fossa Breadth	Choanal Height	Choanal Alare Breadth
Y002	EAM	71.21	51.91	28.38	46.27	41.03	23.20	32.46
Y003	EAF	57.63	45.00	26.30	42.51	33.23	19.03	27.38
Y004	AAF	72.66	52.87	24.86	50.59	30.37	23.40	27.15
Y005	EAF	60.56	46.09	24.25	43.67	40.29	24.23	35.90
Y012	AAF	67.04	49.40	26.67	44.46	31.44	21.80	28.33
Y013	AAM	65.16	50.18	26.06	44.82	42.60	22.69	30.99
Y015	AAM	67.16	47.76	26.64	46.23	43.23	18.81	33.11
Y023	EAM	63.05	52.06	26.21	43.30	32.40	22.00	33.40
Y045	EAF	70.93	52.63	28.95	46.69	47.79	25.01	40.81
Y055	EAM	74.48	57.95	27.56	54.65	33.04	28.16	29.76
Y056	AAF	67.14	52.14	22.60	47.65	31.45	22.37	24.30
Y071	EAF	63.21	46.15	22.81	44.28	31.67	21.91	29.83
Y083	EAM	65.09	48.03	21.25	44.39	29.46	19.99	28.28
Y087	EAM	61.83	49.86	24.03	46.29	32.87	22.20	27.35
Y093	EAF	NA	51.37	22.99	44.63	29.13	20.95	27.89
Y101	EAF	68.31	49.78	21.06	43.30	30.69	22.93	29.76
Y105	AAF	67.24	51.21	24.83	48.15	34.22	24.57	28.62
Y109	AAF	67.12	51.29	23.31	46.31	30.16	21.25	26.10
NM304	AAM	NA	45.76	21.80	38.88	28.29	19.58	24.39
NM030	AAM	59.44	44.73	22.29	41.58	31.57	19.65	25.35

TABLE E11: Results of statistical significance testing for linear measurements

		Nasion to Prosthion	External Nasal Height	Internal Nasal Height	Choana Height	Nasal Alare Breadth	Inferior Nasal Fossa Breadth	Choana Alare Breadth
Hot-Humid Female	Mean	65.64	18.85	44.86	21.11	26.81	38.31	30.45
	Median	67.04	49.4	44.82	21.8	26.64	41.03	30.99
	Z- Value					2.40		
Hot-Humid Male	Mean	66.8	50.91	46.06	23.66	26.07	37.71	34.32
	Median	66.99	52.35	45.18	23.82	25.54	36.35	34.65
	Z- Value					1.32		
Cold-Dry Female	Mean	63.99	48.07	43.66	21.44	22.43	31.09	26.83
	Median	63.21	47.97	43.79	22.06	22.45	31.51	26.35
	Z- Value					-2.89		
Cold-Dry Male	Mean	68.48	51.97	47.63	22.98	23.99	31.20	28.13
	Median	67.18	51.29	46.31	21.25	23.31	30.16	28.28
	Z- Value					-0.57		
p- value		0.64	0.19	0.31	0.22	0.008	0.096	0.07

Bold Z-values are significant by Dunn's Test ($z > 1.960$), Italicized are also significant by Bonferroni Test ($z > 2.6383$)

TABLE E12: Resulting Z-values from the post hoc Dunn's Test.

		HHF	HJM	CDF	CDM
Nasal Passage PC1	AAF	0			
	AAM	1.3607	0		
	EAF	1.74	0.2182	0	
	EAM	3.1537	1.6126	1.5539	0
Nasal Passage PC2		HHF	HJM	CDF	CDM
	AAF	0			
	AAM	2.7465	0		
	EAF	0.8095	2.0949	0	
Nasal Passage Centroid Size	EAM	0.9087	1.8898	0.1396	0
		HHF	HJM	CDF	CDM
	AAF	0			
	AAM	0.9701	0		
Craniofacial Surface PC2	EAF	0.7165	1.6803	0	
	EAM	2.245	1.1465	3.0613	0
		HHF	HJM	CDF	CDM
	AAF	0			
Facial Surface PC1	AAM	0.3402	0		
	EAF	2.3913	2.5968	0	
	EAM	2.7795	2.9607	0.5118	0
		HHF	HJM	CDF	CDM
Nasal Alare Breadth	AAF	0			
	AAM	1.1339	0		
	EAF	1.8144	2.8805	0	
	EAM	2.6192	3.6033	0.9212	0
		HHF	CDM	CDF	CDM
	AAF	0			
	AAM	0.504	0		
	EAF	3.1636	2.444	0	
	EAM	1.8174	1.2095	1.2655	0

Bold Z-values are significant by Dunn's Test ($z > 1.960$), Italicized are also significant by Bonferroni Test ($z > 2.6383$)

REFERENCES

- Aboglaide, O., A. Nazri, R. Yaakob, A. A. Chani, Y. K. Cheah. (2020). Morphometric approach to 3D soft-tissue craniofacial analysis and classification of ethnicity, sex, and age. *PLoS ONE* 15(4).
- Adams, D. C., F.J. Rohlf, D.E. Slice. (2012). A field comes of age: geometric morphometrics in the 21st century. *Hystrix, the Italian Journal of Mammalogy*. 24(1): 7-14.
- Adams, D., M. Collyer, A. Kaliontzopoulou, E. Baken (2021). “Geomorph: Software for geometric morphometric analyses. R package version 3.3.2.
- Bastir, M., I. Megia, N. Torres-Tamayo, D. Garcia-Martinez, F. M. Piqueras, M. Burgos, (2019). Three-dimensional analysis of sexual dimorphism in the soft tissue morphology of the upper airways in a human population. *American Journal of Physical Anthropology*. 171: 65-75
- Bastir M. I., P. Godoy, A. Rosas. (2011). Common Features of Sexual Dimorphism in the Cranial Airways of Different Human Populations. *American Journal of Physical Anthropology*. 146:414-422.
- Bastir, M. I., A. Rosas. (2013). Cranial Airways and the Integration Between the Inner and Outer Facial Skeleton in Humans. *American Journal of Physical Anthropology*. 152:287-293.
- Beule, A. G. (2010). Physiology and pathophysiology of respiratory mucosa of the nose and the paranasal sinuses. *GMS Current Topics on Otorhinolaryngology- Head and Neck Surgery*, 9, Doc07.
- Bookstein, F. L. (2004). Geometric Morphometrics for Biologists.
- Bookstein, F. L. (2014). The relation between geometric morphometrics and functional morphology, as explored by Procrustes interpretation of individual shape measures pertinent to function. *The Anatomical Record* 298:314-327.
- Byun, S., S.K. Chung, & Y. Na. (2019). Air-conditioning characteristics in nasal cavity models exhibiting nasal cycle states. *Journal of Thermal Biology*, 83, 60-68.
- Cardini, A., K. Seetah, G. Barker (2015). How many specimens do I need? Sampling error in geometric morphometrics: testing the sensitivity of means and variances in simple randomized selection experiments. *Zoomorphology*. 134: 149-163.
- Carey, J. W., A. T. Steegman, Jr. (1981). Human Nasal Protrusion, Latitude, and Climate. *American Journal of Physical Anthropology*. 56:313-319.

- Churchill, S. E., L. L. Shackelford, J. N. Georgi, & M. T. Black. (2004). Morphological variation and airflow dynamics in the human nose. *American Journal of Human Biology*, 16(6), 625-638.
- Cole, P. (1988). Modification of Inspired Air. In: Mathew, O.P. , Sant'Ambrogio, G. , eds. *Respiratory function of the upper airway*. New York: Dekker, 415- 439
- Cole, P. (2000). Biophysics of Nasal Airflow: A review. *American Journal of Rhinology*. 14, 245-249.
- Cooke, S. B., C. E. Terhune. (2014). Form, Function, and Geometric Morphometrics. *The Anatomical Record*. 298(1).
- Dallimore, N. S. & R. Eccles. (1977). Changes in human nasal resistance associated with exercise, hyperventilation, and rebreathing. *Acta Oto-Laryngologica*, 84(1-6), 416-421.
- Doorly D. J., D. J. Taylor, R. C. Schroter. (2008). Mechanics of airflow in the human nasal airways. *Respiratory Physiology and Neurobiology*.163(1-3), 100-10.
- Eccles, R. (1978). The central rhythm of the nasal cycle. *Acta Oto-Laryngologica*, 86(5-6), 464-468.
- Evteev, A., A. L. Cardini, I. Morozova, & P. O'Higgins. (2014). Extreme climate, rather than population history, explains mid-facial morphology of Northern Asians. *American Journal of Physical Anthropology*, 153(3), 449-462.
- Franciscus, R. G., & J. C. Long. (1991). Variation in human nasal height and breadth. *American Journal of Physical Anthropology*, 85(4), 419-427.
- Gunz, P., P. Mitteroecker. (2012). Semilandmarks: a method fro quantifying curves and surfaces. *Hystrix, the Italian Journal of Mammalogy*. 24(1), 103-109.
- Hall, R. L. (2005). Energetics of nose and mouth breathing, body size, body composition, and nose volume in young adult males and females. *American Journal of Human Biology: The Official Journal of the Human Biology Association*, 17(3), 321-330.
- Hasegawa, M., & E. B. Kern. (1978). The effect of breath holding, hyperventilation, and exercise on nasal resistance. *Rhinology*, 16(4), 243-249.
- Holton, N. E., T.R. Yokley, A. W. Froehle, & T. E. Southard. (2014). Ontogenetic scaling of the human nose in a longitudinal sample: implications for genus Homo facial evolution. *American Journal of Physical Anthropology*, 153(1), 52-60.
- Keustermans, W., T. Huysmans, B. Schmelzer, J. Sijbers, J. JJ. Dirckx. (2020). The effect of nasal shape on the thermal conditioning of inhaled air: Using clinical tomographic data to build a large-scale statistical shape model. *Computers in Biology and Medicine* 117, 1-13.
- Leong S.C., X. B. Chen, H. P. Lee, D.Y. Wang. A review of the implications of computational fluid dynamic studies on nasal airflow and physiology. *Rhinology*. 2010;48(2), 139-145.
- Liu, T., D. Han, J. Wang, J. Tan, H. Zang, T. Wang, S. Cui. (2012). Effects of septal deviation on the airflow characteristics: using computational fluid dynamics models. *Acta Oto-Laryngologica*, 132(3), 290-298.

- Maddux, S. D., L. N. Butaric, T. R. Yokley and R. G. Franciscus (2017). Ecogeographic variation across morphofunctional units of the human nose. *American Journal of Physical Anthropology*. 162(1), 103-119.
- Marks, T. N., S. D. Maddux, L. N. Butaric, & R. G. Franciscus. (2019). Climatic adaptation in human inferior nasal turbinate morphology: Evidence from Arctic and equatorial populations. *American Journal of Physical Anthropology*, 169(3), 498-512.
- Martonen, T. B., L. Quan, Z. Zhang, & C. J. Musante. (2002). Flow simulation in the human upper respiratory tract. *Cell Biochemistry and Biophysics*, 37(1), 27-36.
- McKeown, A. H., R. W. Schmidt (2012). Chapter 12: Geometric Morphometrics. *Research Methods in Human Skeletal Biology*, 325-359.
- Mitteroecker, P., P. Gunz, S. Windhager, K. Schaefer. (2013). A brief review of shape, form, and allometry in geometric morphometrics with applications to human facial morphology. *Hystrix, the Italian Journal of Mammalogy*. 24(1), 59-66.
- Moore, K. L., A. M. R. Agur, & A. F. Dalley. (2011). *Essential clinical anatomy*. Baltimore, MD: Lippincott Williams & Wilkins.
- Mygind, N., & R. Dahl. (1998). Anatomy, physiology and function of the nasal cavities in health and disease. *Advanced Drug Delivery Reviews*, 29(1-2), 3-12.
- Mlynski, G. H., S. Grutzenmacher, S. Plontke, B. Mlynski, C. Lang (2001). Correlation of nasal morphology and respiratory function. *Rhinology*, 39, 197-201.
- Mlynski, G. H. (2013). Physiology and Pathophysiology of Nasal Breathing. *Nasal Physiology and Pathophysiology of Nasal Disorders*. Chapter 20, 257-269
- Naftali, S., M. Rosenfeld, M. Wolf, & D. Elad. (2005). The air-conditioning capacity of the human nose. *Annals of Biomedical Engineering*, 33(4), 545-553.
- NCSS 11 Statistical Software. (2016). NCSS, LLC. Kaysville, UT, ncss.com/software/ncss
- Noback, M. L., K. Harvati, & F. Spoor. (2011). Climate-related variation of the human nasal cavity. *American Journal of Physical Anthropology*, 145(4), 599-614.
doi:10.1002/ajpa.21523
- Sahin-Yilmaz, A., R. Naclerio. (2011). Anatomy and Physiology of the Upper Airway. *Proceedings of the American Thoracic Society*. 8, 31-39.
- Thai, Elizabeth. (2020). Evaluating Ecogeographic Variation in the Human Nasal Passages Using In-Silico Decongestion of the Nasal Cycle. Master of Science in Medical Sciences-Anatomy. The University of North Texas Health Science Center. May 2020. 49pp.
- ThermoFisher Scientific AVIZO Fire 8.1. (2014). ThermoFisher Scientific. <https://www.thermofisher.com/us/en/home/industrial/electron-microscopy/electron-microscopy-instruments-workflow-solutions/3d-visualization-analysis-software.html>
- Walker, J. E. C., & R. E. Wells Jr. (1961). Heat and water exchange in the respiratory tract. *Amer. J. Med.*, 30(2), 259-267.
- Webster, M., & H. D. Sheets (2010). A Practical introduction to landmark-based geometric morphometrics. *The Paleontological Society Papers*. Volume 16, 163-188.

- Yokley, T. R. (2009). Ecogeographic variation in human nasal passages. *American Journal of Physical Anthropology*, 138(1), 11-22.
- Zaidi, A. A., B. C. Mattern, P. Claes, B. McEvoy, C. Hughes, & M. D. Shriver. (2017). Investigating the case of human nose shape and climate adaptation. *PLoS Genetics*, 13(3).
- Zelditch, M. L., D. L. Swiderski, H. D. Sheets, W. L. Fink (2004). Geometric Morphometrics for Biologists: A primer.